Universidade de Aveiro
2011

Departamento de Física

Mariana Vieira Lima Matias da Rocha

Modelação numérica do impacto dos esporões na hidrodinâmica costeira

Numerical modelling of groin impact on nearshore hydrodynamics

Dissertação apresentada à Universidade de Aveiro para cumprimento dos requisitos necessários à obtenção do grau de Mestre em Meteorologia e Oceanografia Física, realizada sob a orientação científica do Prof. Dr. Carlos Daniel Borges Coelho, Professor Auxiliar do Departamento de Engenharia Civil da Universidade de Aveiro e da Dra. Conceição Juana Espinosa Morais Fortes, Investigadora Principal do Laboratório Nacional de Engenharia Civil.

Este trabalho foi desenvolvido no âmbito do projecto BRISA: BReaking waves and Induced SAnd transport (PTDC/ECM/67411/2006), com o apoio financeiro da Fundação para a Ciência e Tecnologia – FCT.

“Waiting for waves is ok. Most people spend their lives waiting for nothing.”

o júri

presidente

Prof. Doutor José Manuel Henriques Castanheira
Professor Auxiliar da Universidade de Aveiro

Prof. Doutor António Alexandre Trigo Teixeira
Professor Associado do Instituto Superior Técnico

Prof. Doutor Carlos Daniel Borges Coelho
Professor Auxiliar da Universidade de Aveiro

Doutora Conceição Juana Espinosa Morais Fortes
Investigador Principal do Laboratório Nacional de Engenharia Civil

acknowledgements

I would now like to thank the help and support of the many people that contributed to the process of writing this thesis.

To both my supervisors,

Prof. Dr. Carlos Coelho, for his support, availability and sympathy since the very beginning and the close follow up of my work;

Dr. Conceição Juana Fortes, for how wonderfully she received me at LNEC, and for her endless patience and will to solve every little problem and doubt which I came across during my stay at LNEC.

To Dr. Richard Gomes, for his great help with the computer clusters where the simulations were run, and Engs. Rui Capitão and Francisco Sancho for the occasional suggestion and correction.

Also, I could never forget thanking all my friends from the NPE - LNEC, for the warm welcome, for making the hardest days easy, for the everyday cheerfulness and fun, support and knowledge exchange and everything else, along these six months of my stay.

Thanks as well to my old friends from Aveiro, for all the moments that make this life even more worthwhile.

And last, but not least, above all, I thank my amazing family, particularly to my parents and brother, for a life-long support in every possible way and for helping me become who I am.

palavras-chave Hidrodinâmica Costeira; Modelação Numérica; COULWAVE; Esporões.

resumo

A hidrodinâmica costeira engloba uma variedade de processos ligados à propagação das ondas em direcção à costa, empolamento e eventual rebentação. Fenómenos como a refracção, difracção, reflexão e a própria rebentação possuem características não lineares, o que dificulta o seu estudo e modelação. A hidrodinâmica influencia também a morfodinâmica das praias, área de investigação em grande foco actualmente.

A modelação numérica constitui uma ferramenta importante na investigação dessas dinâmicas e fenómenos envolvidos. Torna-se, então, necessário calibrar os modelos para que sejam capazes de representar correctamente os processos que actuam na costa e simular alterações futuras.

Numa primeira fase desta tese, resultados obtidos com o modelo COULWAVE são comparados com dados de campo de alturas significativas de onda e de velocidades horizontais, recolhidos na praia da Cornélia, na Costa da Caparica. Os resultados são bastante promissores, particularmente para as alturas significativas de onda medidas antes da rebentação.

Os esporões são estruturas transversais à costa projectadas para reter sedimentos em transporte na corrente de deriva litoral, com o objectivo de minorar a erosão em trechos específicos da linha de costa. Estas estruturas são frequentemente colocadas em costas arenosas e têm associado um importante impacto na hidro e morfodinâmica costeira, uma vez que se estendem perpendicularmente à costa, em direcção ao largo. Diversos constrangimentos estruturais e ambientais, entre os quais o comprimento e orientação do esporão, a altura das ondas incidentes e o nível da superfície do mar, determinam esse impacto.

Neste contexto, a segunda fase desta tese consiste na avaliação, através da modelação numérica com o já referido modelo COULWAVE, do impacto dos esporões na altura significativa das ondas e velocidade horizontal junto à costa, considerando diferentes cenários. Os vários cenários correspondem a diferentes comprimentos (L=200 m, L=250 m, L=300 m e L=400 m) e orientações ($\phi = 10º$, $\phi = 15º$, $\phi = 25º$ e $\phi = 30º$) do esporão, diferentes alturas significativas das ondas incidentes (Hs=1 m, Hs=1.5 m, Hs=2.0 m e Hs=3.0 m) e diferentes níveis da superfície do mar (SSL=0.50 m, SSL=0.75 m, SSL=1.50 m e SSL=2.40 m). Verifica-se que a altura das ondas incidentes é o factor que adquire uma maior relevância no impacto do esporão na hidrodinâmica costeira, seguido do nível da superfície do mar, comprimento do esporão e, finalmente, da orientação do esporão.

keywords

Nearshore Hydrodynamics; Numerical Modelling; COULWAVE; Groins.

abstract

Nearshore hydrodynamics involves a variety of processes as waves propagate towards the coast, start shoaling and eventually break. Phenomena such as refraction, diffraction, reflection and the breaking itself are highly nonlinear, and thus difficult to study and model. The hydrodynamics will further play a role on the morphodynamics of beaches, a subject undergoing intensive research nowadays.

Numerical modelling presents a useful tool to investigate these dynamics and involved phenomena. It is then necessary to calibrate models to accurately represent the processes acting on the coast and be able of simulating future changes.

This thesis begins with the comparison of COULWAVE model results with field data from Cornélia beach, in Costa da Caparica, for both significant wave height and horizontal velocity. Results are quite promising, especially for significant wave height values measured before wave breaking.

Groins are cross-shore structures projected to retain sediments from the longshore drift, to attenuate the erosion of specific coastline stretches. Frequently employed in sandy coasts, these structures are expected to have an important impact on nearshore hydrodynamics and morphodynamics, as they extend seawards, approximately perpendicularly to the coast. Several structural and environmental factors condition that impact, such as groin length and orientation relatively to the shoreline, and incident wave height and sea-surface level.

Hence, in the second phase of this thesis, it is performed an evaluation, through numerical modelling with COULWAVE model, of the impact of groins in significant wave height and horizontal velocity nearshore, under different scenarios. The different scenarios assumed different groin lengths (L=200 m, L=250 m, L=300 m and L=400 m) and orientations (ϕ =10º, ϕ = 15º, ϕ = 25º and ϕ = 30º), different significant heights of incident waves (Hs=1.0 m, Hs=1.5 m, Hs=2.0 m and Hs=3.0 m) and different sea-surface levels (SSL=0.50 m, SSL=0.75 m, SSL=1.50 m e SSL=2.40 m). Incident wave height is found to be a preponderant factor on groin impact in nearshore hydrodynamics, followed by sea-surface level, groin length and, finally, groin orientation.

Contents

LIST OF FIGURES

LIST OF TABLES

1. INTRODUCTION

1.1. Motivation

Beaches are remarkably complex and dynamic environments, difficult to survey and model. The panoply of processes in action, inducing changes on a variety of different temporal and spatial scales, ranging from the tiniest small-scale turbulence phenomena, to large-scale beach erosion, contribute for this research topic being such a challenging and fascinating one.

Wind-generated waves have been recognised as a major forcing agent on hydrodynamics and morphodynamics of coastal areas, particularly across the surf zone, as wave breaking often induces energy dissipation, sediment transport and momentum exchange between waves and near-shore currents. In the shallow waters of coastal zones, the shoreward wave propagation and consequent shoaling, generally involves complex nonlinear phenomena, such as refraction, diffraction, wave breaking and runup, which are of fundamental importance in coastal and ocean engineering (Dong and Zhan, 2009). Hence, the ability to describe, simulate and forecast wave propagation, shoaling and breaking, becomes an essential matter for the understanding of nearshore and surf zone dynamics.

Facing the North Atlantic, the West Portuguese coast has a highly energetic wave climate, with wave heights that may exceed 7 m and wave periods that can be higher than 17 s during major storm events. The most frequent NW wave direction induces an important N-S longshore drift that plays a crucial role on longitudinal sediment transport, which is in turn related to beach erosion, as it transports most of the sediments that nourish the beaches (Costa, 2001). Together with the shoreline natural adjustment, aiming to smooth the coastline, human action, such as hydropower generation, implying the construction of damns on major rivers, and shoreline-protection engineering solutions, implying the building of cross-shore structures, like groins and breakwaters, also contribute to the weakening and trapping of sediments that remain then kept from drifting alongshore.

Groins are cross-shore structures projected to retain sediments from the longshore drift, to attenuate the erosion of specific coastline stretches. The shoreline adjusts to the presence of the obstruction in longshore sediment transport, and after some time, accretion causes a positive increase in beach width updrift of the groin. Conservation of sand mass then produces erosion and decrease in beach width on the downdrift side of the groin. Downdrift shoreline retreat may be permanent and irreversible or temporary and reversible, if some years after the construction of the groin the alongshore sediment transport resumes again (Basco, 2006). The real impact of groins on the wave conditions and the velocity field near-shore is still an ongoing field of investigation and thus requires further research.

1.2. Aims

The two main objectives of this thesis are:

- The application of COULWAVE numerical model to wave propagation, shoaling and breaking in Cornélia beach, in Costa da Caparica, Portugal, in order to evaluate its performance;
- The study of groin impact on significant wave height and horizontal velocity nearshore, accounting for different groin lengths and orientations relatively to the coast, different incident wave heights and tide levels.

Both aims wish to improve current knowledge on the simulation of nearshore hydrodynamics, with a particular model, COULWAVE, and the influence of groins on such phenomena.

1.3. Thesis structure

This work starts with a brief state of the art on modelling wave shoaling and breaking and a general approach to some studies conducted about groin impact on wave height and horizontal current velocities. It then follows with the characterization of the numerical model employed, just before the description of the field campaign and instruments used for the *in situ* data collection.

Afterwards, the main focus of this work is presented: the model application to the field case – Cornélia beach, Costa da Caparica. This chapter begins with a depiction of the model conditions for the numerical simulations and a comparison between numerical results and field data to evaluate the performance of the model. Then the application of the model for studying groin impact on wave height and horizontal velocity nearshore, is described.

This work draws to a close with the conclusions and some future improvements are suggested.

2. STATE OF THE ART

2.1. Modelling wave shoaling and breaking

Wave propagation from deeper waters into shallow coastal waters, transforms near-symmetrical sinusoidal shaped waves, to skewed, pitched-forward, tooth-swath shaped waves, that eventually break, and non-linear phenomena such as refraction, diffraction and breaking acquire a preponderant relevance.

Shallow-water wave models are based on the classical uniform-depth theories of Boussinesq (1872) and Korteweg and deVries (1895), extended to variable depth by Peregrine (1967), in which the frequency dispersion of wave propagation in intermediate depths was poorly described and the weakly nonlinear assumption limited the largest wave height that could accurately be modeled. Both the weak dispersion and nonlinearity limited the validity of the models to very shallow water. Recent advances include high-order dispersion effects (Madsen *et al.*, 2003), which improve the dispersion properties of the models, and a high-order numerical scheme developed by Wei *et al.* (1995) that allows full nonlinearity. More recent advances include the works by Chen *et al.* (2000), Chen *et al.* (2003), Watts *et al.* (2003) and Shi and Kirby (2005), among others (Cavaleri *et al.*, 2007; Lynett *et al.*, 2002).

According to Cavaleri *et al.* (2007), shallow-water wave propagation models can generally be considered either determinist or stochastic. Time-domain (physical domain) and spectral-domain (complex amplitude evolution) Boussinesq models are deterministic (phase resolving) models, since they are able of resolving the phases of the individual waves. These models are usually derived from the Euler equation for potential flows (Laplace equation plus boundary conditions) under the hypothesis of weak nonlinearity and in the limit of shallow water ($kh \rightarrow 0$, where k is the wave number and h the water depth).

One example of a Boussinesq-type model is the COULWAVE model (Lynnet and Liu, 2002), which is a time-domain deterministic model. This type of models is typically applied to domains with spatial scales of the order of tens of wavelengths, since they are so computationally demanding that larger scale applications become prohibitive. Also, the needed phase-resolving

boundary conditions are often not available and wave field statistics, as opposed to the details of a single realization, become necessary. This implies the computation of a multitude of realizations, thus increasing computational and time expenses. Despite recent advances in Boussinesq modelling, this computational cost severely limits the use of such models for operational nearshore wave prediction, particularly when only limited computational resources are available (Cavaleri *et al.*, 2007).

2.2. Groin impact on wave shoaling and breaking

Groins are the oldest and most common shore-connected, beach stabilization structures. Being probably the most misused and improperly designed of all coastal structures, they are usually perpendicular or nearly at right angles to the shoreline and relatively short compared to navigation jetties at tidal inlets (Basco, 2006). Still according to Basco (2006), although groins have been around a long time and many references exist, most only provide a few rules of thumb. Currently, no systematic methods for functional design under a wide range of structural shapes, waves and sediment transport conditions exist (Basco, 2006).

Waves breaking alongshore at an angle create a time-averaged current and sediment transport. The presence of a groin simply blocks a part of this normal transport of sand alongshore, by the local, wave-induced current. Wave diffraction causes reduced wave energy in the lee of the groin relative to the midcompartment, mean water-level setup gradients, and setup induced currents behind the groin. These contribute to complex current circulation patterns that move sediment alongshore and offshore along the lee-side of the groin (Dean, 1978). The strength of these internal current patterns depends on groin planform geometry, but also on groin cross-section elevation and permeability across the surf zone. Waves diffract around the groin tip, propagate over the submerged section and reflect off the body of the groin. These interactions vary with water depth changes during the tidal cycle (Basco, 2006).

Pattiaratchi *et al.* (2009) argue that the interaction between the hydrodynamics field in wave-dominated waters has usually been examined only in the laboratory or through numerical studies, but few field studies have been conducted. Hence, in their study, these authors employed surf zone drifters and a current meter in order to study the nearshore circulation patterns in the lee of groins, which are known to affect local sediment transport rates, especially downdrift erosion. The data were then used in a circulation model. Bowen and Inman (1969), using a resonant condition for standing waves in a wave basin, demonstrated that when waves approach a groin at an angle, wave diffraction and refraction produce smaller waves in the lee of the groin. This results in a wave set-up field that produces a longshore current flowing towards the groin, which then reflects it offshore, originating an adjacent rip-current. Pattiaratchi *et al.* (2009) found this longshore current to diverge at the limit of the geometric shadow of the groin: in the region between the divergence point and the groin, the longshore current flowed towards the groin; beyond the divergence point, it flowed away from it. This divergence point is a consequence of the change in the wave set-up gradient between the exposed surf zone and the sheltered region in the geometric shadow of the groin. The alongshore variation in the wave-setup has previously been demonstrated by Gourlay (1974) to be the driving force of this current system. Furthermore, as usually verified in wave-generated current systems, this particular current system also proved to respond to forcing frequencies that correspond to variations in the incident wave climate (Pattiaratchi *et al.*, 2009).

In the Pattiaratchi *et al.* (2009) study, the divergence point was found to move further offshore responding to larger waves, whereas small waves had the opposite effect. Small changes in the wave height, direction and period had a minor effect on the location of the divergence point.

According to Pattiaratchi *et al.* (2009), the four main characteristics of this current system can be described as ensuing:

- an initial broad, onshore inflow in the exposed region of the shore due to Stokes drift and mass transport of breaking waves;
- a longshore current, flowing from the exposed surf zone towards the groin;
- a rip-current along the leeward face of the groin;
- a deflection in the direction of the incident waves at the seaward extent of the rip-current where the flow continued alongshore before turning shoreward, in contrast with classic rip-currents that normally show a seaward extent marked by a cloud of sediment-laden water that denounces where the current disperses.

Higher rip-current speeds are thought to result in an increased wave height and consequent prolongation of the offshore extent of the current adjacent to the groin. The influence of the rip-current resulting from the deflection of the longshore current by the groin, on the updrift side, has been suggested as one of the possible reasons for the failure of the groins as shore protection structures. Pattiaratchi *et al.* (2009) further measured that 55 % of the currents along the lee-side of the groin, including the strongest currents, were directed offshore. Thus, the results reported in this study seem to support the idea that a rip-current with a potential for offshore transport of sediment may also be present in the lee-side of groins. These authors support, then, that the presence of an eddy system in the lee of a groin can provide a mechanism for beach erosion downdrift of the structure, through the offshore transport of sediments via the rip-current adjacent to the groin (Pattiaratchi *et al.*, 2009).

It has hence become clear, from all the above, that groins have an important impact on nearshore hydrodynamics and morphology and several factors that will condition this impact should be accounted for.

Prevailing water levels will determine where wave-forces act on the structure and where the erosive action of waves will be felt on the beach profile. Furthermore, since a groin extends across the surf zone, different elements of the structure are submitted to critical design conditions at different water levels. Thus, different water levels should be considered when groin impact is being evaluated. For e.g., at low water level, the seaward-end of the groin might experience breaking waves, while more landward sections experience broken waves, whereas at a higher water level, a more landward section of the groin might experience breaking waves, and the seaward end experience non-breaking waves. The location on a structure where a wave of given height and period breaks, depends on the water depth and nearshore slope. Thus, there will often be a critical water level where maximum wave effects occur (U. S. Army Corps of Engineers, 1992).

Wave height statistics are also needed to determine the level of wave action to which various portions of a groin will be subjected. Since groins are located very close to the shore, waves along the shoreward portion of the groins are depth limited and waves along their seaward-end, may or may not be depth limited, depending on the prevailing water depth and height of incident waves. Moreover, the predominant wave direction determines shoreline orientation, since it tends to align nearly parallel to the incoming wave crests. Nearshore bathymetry will also be important, as it conditions wave propagation, shoaling, refraction and diffraction, phenomena that will alter local wave heights and directions (U. S. Army Corps of Engineers, 1992).

3. NUMERICAL MODEL: COULWAVE

3.1. Brief description

COULWAVE (Cornell University Long and Intermediate Wave Modelling Package), a numerical model initially developed by Lynett and Liu (2002), based upon the extended Boussinesq-type equations deducted by Wei *et al.* (1995), allows for the evolution of fully nonlinear and dispersive waves over variable bathymetry.

The model equations are deducted from depth-integration of continuity and momentum equations, using a multi-layer concept, which considers the division of the water column in layers, each with a determined vertical velocity profile. The accuracy of the model is thus dependent on the number of layers considered and its applicability extends to very deep waters, as it continues to present linear characteristics up to $kh{\sim}8$ and a second order nonlinear behaviour up to $kh{\sim}6$ (where k is the wave number and h, the water depth).

For the one-layer model, as it will be used in this work, the continuity and momentum equations can be written as:

$$\frac{1}{\varepsilon_0}\frac{\partial h}{\partial t}+\frac{\partial \zeta}{\partial t}+\nabla\cdot[(\varepsilon_0\zeta+h)\overrightarrow{u_1}] -\mu_0^2\nabla\cdot\left\{\left[\frac{\varepsilon_0^3\zeta^3+h^3}{6}-\frac{(\varepsilon_0\zeta+h)\kappa_1^2}{2}\right]\nabla S_1+\left[\frac{\varepsilon_0^2\zeta^2-h^2}{2}-(\varepsilon_0\zeta+h)\kappa_1\right]\nabla T_1\right\}=O(\mu_0^4)\ ; \tag{1}$$

$$\frac{\partial \overrightarrow{u_1}}{\partial t}+\varepsilon_0\overrightarrow{u_1}\cdot\nabla\overrightarrow{u_1}+\nabla\zeta+\mu_0^2\frac{\partial}{\partial t}\left\{\frac{\kappa_1^2}{2}\nabla S_1+\kappa_1\nabla T_1\right\} +\varepsilon_0\mu_0^2\left[(\overrightarrow{u_1}\cdot\nabla\kappa_1)\nabla T_1+\kappa_1\nabla(\overrightarrow{u_1}\cdot\nabla T_1)+\kappa_1(\overrightarrow{u_1}\cdot\nabla\kappa_1)\nabla S_1+\frac{\kappa_1^2}{2}\nabla(\overrightarrow{u_1}\cdot\nabla S_1)\right] +\varepsilon_0\mu_0^2\left[T_1\nabla T_1-\nabla\left(\zeta\frac{\partial T_1}{\partial t}\right)\right]+\varepsilon_0\mu_0^2\nabla\left(\zeta S_1T_1-\frac{\zeta^2}{2}\frac{\partial S_1}{\partial t}-\zeta\overrightarrow{u_1}\cdot\nabla T_1\right) +\varepsilon_0\mu_0^2\nabla\left[\frac{\zeta^2}{2}(S_1^2-\overrightarrow{u_1}\cdot\nabla S_1)\right]=O(\mu_0^4); \tag{2}$$

where

$$\mu_0=\frac{h_0}{l_0};\qquad \kappa_1=\alpha_1h+\beta_1\zeta;\qquad S_1=\nabla\cdot\overrightarrow{u_1}\ ;$$
$$T_1=\nabla\cdot(h\overrightarrow{u_1})+\frac{1}{\varepsilon_0}\frac{\partial h}{\partial t};\qquad \varepsilon_0=\frac{a_0}{h_0};$$

and ζ is the free-surface elevation, ε is the nonlinearity parameter, μ the frequency-dispersion parameter and S_1 a shape factor. The index one relates to the one-layer considered and the index zero is used for the characteristic parameters that do not depend on the number of layers. $\overrightarrow{u_1}$ is the horizontal velocity vector at a defined depth z_1 (herein $z_1=-0.531h$, recommended by Nwogu (1993) and adopted by most researchers), h_0 is the characteristic or baseline water depth (function of space), l_0 is the characteristic wavelength and a_0 the wave amplitude, the coefficients α_1 and β_1 are arbitrary and user defined, t is the time variable, $\frac{\partial}{\partial t}$ is the partial derivative with respect to t and ∇ is the gradient of a scalar function and the velocity vector in the only considered layer, $\vec{U}_1$, is given as:

$$\vec{U}_1=\overrightarrow{u_1}-\mu_0^2\left\{\frac{z_1^2-k_1^2}{2}\nabla S_1+(z_1-k_1)\nabla T_1\right\}+O(\mu_0^4). \tag{3}$$

For the numerical exterior boundaries two types of conditions are applied: reflection and radiation. The reflective, or no-flux boundary condition follows the work of Wei and Kirby (1995) and for the radiation, or open boundary condition, a sponge-layer is applied, in the manner recommended by Kirby *et al.* (1998).

Lynett and Liu (2004) further introduced additional terms in the equations in order to account for bottom friction, wave breaking and wave generation inside the domain and added time-dependent water depth terms, in order to consider bottom-profile time variations induced by landslides and earthquakes.

Bottom friction ($\overrightarrow{R_f}$) and wave breaking ($\overrightarrow{R_b}$) are the two forms of physical dissipation considered, and modify the momentum equation according to (4):

$$\frac{\partial \overrightarrow{u_1}}{\partial t} + \cdots + \overrightarrow{R_f} - \overrightarrow{R_b} = 0 \tag{4}$$

To solve the equations, a high-order predictor-corrector scheme is utilized, employing a third order in time explicit Adams-Bashforth predictor step and a fourth order in time Adams-Moulton implicit corrector step with an accuracy of Δt^4 (Press *et al.*, 1989). Finite differences are used to approximate spatial derivatives, with an accuracy of Δx^4 (note that more recent versions of the model also allow the use of the finite-volumes method).

3.2. Breaking scheme

Since wave breaking is the most relevant physical dissipation phenomenon in this work, it will be now explained in further detail.

The breaking scheme employed by Lynett and Liu (2002) follows the work of Kennedy *et al.* (2000) and Chen *et al.* (2000), and is developed from an "eddy viscosity" approach, where a user-defined formulation for eddy viscosity is part of a momentum conserving, *ad hoc*, dissipative term, $\overrightarrow{R_b}$, with components R_{bx} and R_{by} as it follows:

$$R_{bx} = \frac{1}{H}\left\{\left[\nu(Hu_1)_x\right]_x + \frac{1}{2}\left[\nu(Hu_1)_y + \nu(Hv_1)_x\right]_y\right\}; \tag{5}$$

$$R_{by} = \frac{1}{H}\left\{\left[\nu(Hv_1)_y\right]_y + \frac{1}{2}\left[\nu(Hv_1)_x + \nu(Hu_1)_y\right]_x\right\}; \tag{6}$$

where indexes x and y represent the spatial derivatives, $H = h + \zeta$ is the total water depth, and ν is the eddy viscosity, given by:

$$\nu = BH\zeta_t \tag{7}$$

The purpose of B is to ensure a smooth transition between breaking and non-breaking states and it can be defined, following Kennedy *et al.* (2000), by:

$$B = \left\{ \begin{array}{ll} \delta, & \zeta_t \geq 2\zeta_t^b \\ \delta\left(\zeta_t/\zeta_t^b - 1\right), & \zeta_t^b < \zeta_t \leq 2\zeta_t^b \\ 0, & \zeta_t \leq \zeta_t^b \end{array} \right\};$$

where δ is an amplification factor and the parameter ζ_t^b determines the onset and cessation of wave breaking and is defined as it follows:

$$\zeta_t^b = \begin{Bmatrix} \zeta_t^{(F)}, & t - t_o \geq T^b \\ \zeta_t^{(I)} + \frac{t - t_o}{T^b}\left(\zeta_t^{(F)}, -\zeta_t^{(I)}\right), & 0 \leq t - t_o < T^b \end{Bmatrix};$$

where $\zeta_t^{(I)}$ is the initial free surface transient threshold that must be exceeded for a breaking event to initiate, $\zeta_t^{(F)}$ is the minimum transient required for a breaking event to continue, t is the local time instant, t_o is the time instant when breaking started, and T^b is a transition time.

From this point, the breaking model by Lynnet and Liu (2002) diverges from the one formulated by Kennedy *et al.* (2000), that described the four free breaking parameters based on the linear long wave speed (i.e. $\zeta_t^{(I)} = 0.65\sqrt{gh}$) , and a description based on the nonlinear long wave speed ($\sqrt{gH}$) is chosen instead, to avoid problems with calculations where $h < 0$ (as when a wave runs up the shoreline). A number of regular wave tests on plane slopes performed by Hansen and Svendsen (1979) allowed the default setting of the free parameters as:

$$\delta = 6.5; \qquad \zeta_t^{(I)} = 0.65\sqrt{gH}; \qquad \zeta_t^{(F)} = 0.08\sqrt{gH}; \qquad T^b = 8.0\sqrt{\frac{H}{g}}.$$

The values of these parameters were defined for smooth plane slopes and should hence be adjusted if bottom profile conditions are different.

4. FIELD DATA

4.1. Field campaign

The field data used in this thesis was acquired during a field campaign, carried out in the scope of a FCT (Fundação para a Ciência e Tecnologia) financed project, BRISA (Breaking Waves and Induced Sand Transport), which comprises three different approaches: physical and numerical modelling, and *in situ* data collection. This project, aiming improving the understanding of wave breaking and its influence on sediment transport, is being conducted by a group of research institutions, namely LNEC (National Civil Engineering Laboratory) and both Algarve and Aveiro Universities.

The campaign was carried out between the 11th and 15th of May, 2010, in the vicinity of Cornélia beach (a beach south of *Praia da Saúde*, Fig. 1), in Costa da Caparica, Portugal, and its main objective was the acquisition of hydrodynamic and morphologic data for later tests and the evaluation of the performance of numerical models. Furthermore, these data contribute to the knowledge on wave breaking and sediment dynamics, and the specific beach site morphodynamics.

During the campaign, several instruments were installed, measuring free-surface elevation (Pressure Transducers, PT), current velocity (Electromagnetic Current Meters, ECM and Acoustic Doppler Velocimeters, ADV) and turbidity and suspended particles concentration (Optical Backscatter Sensors, OBS). All the instruments were positioned during low-tide, the positions calculated using a DGPS, georeferenced through a TRK-DGPS system, and synchronized with Lisbon Astronomical Observatory.

Furthermore, data from a topo-bathymetric survey performed on the first day of the campaign, during daytime high-tide, allowed the construction of a digital model of the terrain (Bezerra and Ferreira, 2010). The domain extends from about 5 m above chart datum (CD) to depths of 7.6 m, further offshore. The beach presents a typical bar-trough profile, with a submersed bar located at about 650 m from the deepest end of the domain, without great alongshore bathymetry changes.

a) b)

Fig. 1 – Location of study area: a) Costa da Caparica field site (Google Earth) and b) Cornélia Beach (Bezerra and Ferreira, 2010).

Fig. 2 presents an estimation of the tide level (referred to CD), obtained by interpolation from high and low tides predicted by the Portuguese Hydrographic Institute, for the period comprised between the 08:30 on the 12-05-2010 and 23:30 on the 14-05-2010.

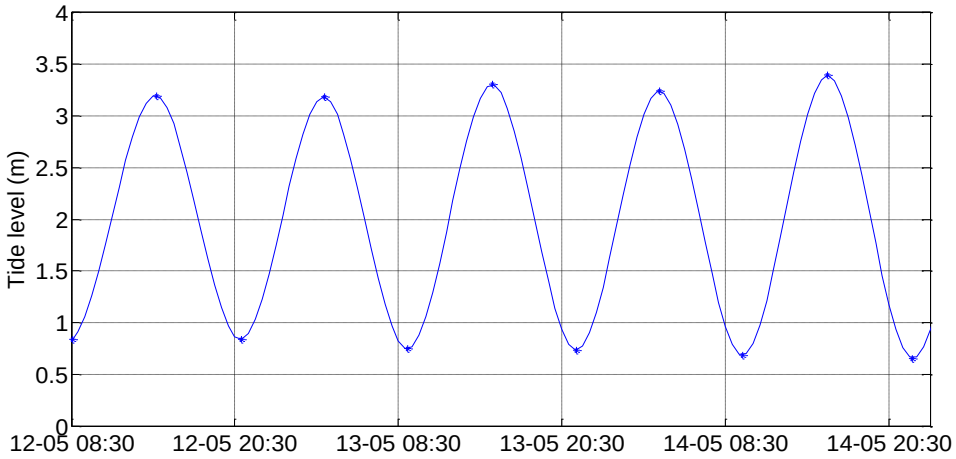

Fig. 2 – Tide level between 08:30, on the 12-05-2010 and 23:30, on the 14-05-2010.

4.2. Data

The *in situ* data collected in the field campaign that is analysed in this work, consist on simultaneous measurements of pressure and horizontal current velocity, acquired with instruments approximately located along the same cross-shore profile, attached to H-shaped structures (as shown in Fig. 3).

Free-surface measurements from three pressure transducers are analysed: one positioned in deeper waters (7.6 m, referred to CD) and two located closer to the shore, in the surf zone. Horizontal velocity was measured along both cross-shore and longshore directions, using a electromagnetic current meter (ECM) located on the surf zone (Table 1).

a) b)

Fig. 3 – a) Location of the beach profile where the instruments where positioned (Google Earth) and b) Beach profile and location of the H-structures used in the field campaign (Bezerra and Ferreira, 2010).

Table 1 – Identification, position and sampling frequency of the instruments.

Structure	Identification	Model	X (Easting) (m)	Y (Northing) (m)	Z (CD) (m)	Sampling Frequency (Hz)
-	PT00	Infinity_WH	-95847.090	-115311.000	-7.6	5
H1	PT01	Infinity_WH	-95357.825	-114985.584	1.506	1 and 10
H1	ECM	Infinity_ECM	-95357.492	-114985.802	1.549	10
H5	PT02	LevelTroll500	-95279.189	-114931.251	3.031	2

The acquisition periods of each instrument are described in Table 2. It should be further noted that for PT01 transducer, during the first of the two periods, the sampling was continuous, but due to an equipment malfunction, possibly associated with software problems, the effective sampling frequency attained was 1 Hz, and not the desired 10 Hz sampling frequency, usually employed with this kind of instruments. The desired frequency was only operating during the second sampling period. Nevertheless, all data were considered for analysis.

Table 2 – PT00, PT01, PT02 and ECM sampling periods.

Instrument	Sampling Period				
PT00	08:14:23, 12-05 until 07:40:00, 15-05				
PT01	08:30, 12-05 until 10:26, 14-05		10:45 until 19:43, 14-05		
PT02	11:00 until 20:00, 12-05	1:00 until 6:00, 13-05	13:30 until 17:30, 13-05	1:00 until 7:00, 14-05	12:30 until 17:30, 14-05
ECM	10:00:00, 12-05 until 9:29:00, 13-05		10:10:00, 13-05 until 22:51:19, 14-05		

For a more detailed description of field data, refer to Bezerra and Ferreira (2010).

5. MODEL APPLICATION TO THE FIELD CASE

5.1. Introduction

In this section, the COULWAVE model is applied to simulate the wave propagation in the vicinity of Cornélia beach, Costa da Caparica, for the incident wave conditions observed between 12th and 14th of May, 2010. Numerical results and field data are compared to evaluate the performance of the numerical model and to calibrate some of its wave breaking parameters.

5.2. Simulation conditions

The incident wave conditions simulated corresponded to regular waves whose characteristics were based on the values measured by PT00 sensor in the Cornélia beach, during the measuring period, between the 12th and the 14th of May, 2010.

A perpendicular direction of incident waves was assumed, since the instruments on the field could not register wave direction.

For each incident wave condition, defined by its significant wave height and significant period, tide level and water depth, the model was run during 300 s (except for the case of spectral analysis, where it was run during 1800 s), and the results were written to file every 1.0 s. Computational and time expenses made it prohibitive running all the simulations much longer.

The domain was discretized in a grid with $\Delta x = \Delta y \approx 2.0$ m, with 900 m along the x-direction and 858 m along the y-direction (Fig. 4). This grid is created by the model based on a minimum number of points per wavelength, set as 30 in the simulations performed, defined according to the wave period. The bathymetry considered to construct the model grid corresponded to an approximation of the real bathymetry.

It was further added a constant-depth zone to the domain, where the referred incident regular waves were generated through the source-function method (Wei *et al.*, 1995). The source-function was located in the position $x = 100$ m. In both left and right open boundaries of the domain, absorption boundary conditions were applied ($l_0/2 = (gT^2)/4\pi$ layers, where l_0 is the wavelength, T the wave period and g the acceleration due to gravity), while the other two boundaries were considered reflective.

It was considered, for all simulations, only one layer, fully-nonlinear equations (with nonlinear dispersive terms), a bottom friction coefficient of 1.0×10^{-2} and a Courant number of 0.4.

Considering $\zeta_t^{(I)} = A\sqrt{gH}$, the default value of A set for a smooth-plane sloping bottom profile is 0.65. However, Chen *et al.* (2000) argued a value of 0.35 for bar-trough profile beaches, as the profile considered in this study. Since diverse groins are to alter the bar-trough profile for each scenario to be studied, and after several attempts of parameter adjustment were made, a value of $A = 0.50$ was assumed in this work, to allow for the greatest number of simulations to run without crashing and conveniently simulate the breaking events.

The values of the parameters not mentioned herein were set as the default values suggested by the manual of the model (Lynnet and Liu, 2002).

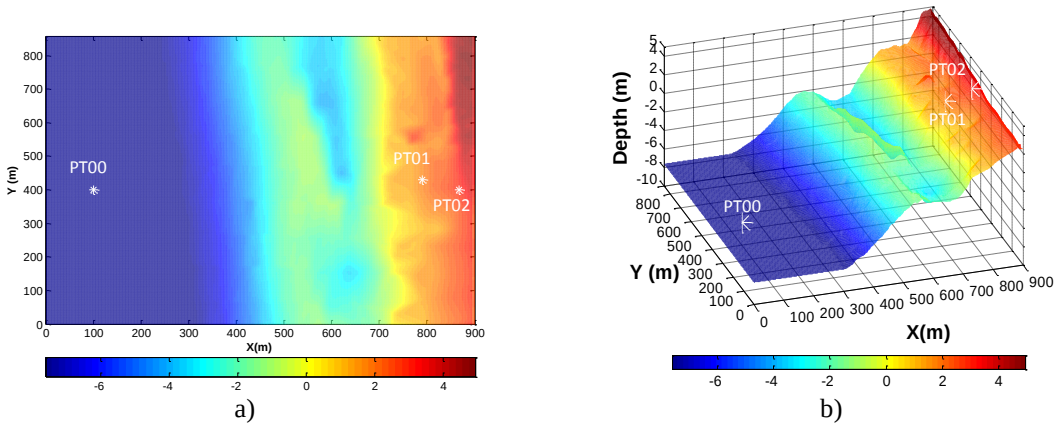

a) b)

Fig. 4 – a) Plan-view of the real domain and bathymetry and b) 3D representation of the domain bathymetry. White markers mark PT00, PT01 and PT02 grid-points location (respectively, from the most offshore location to the beach). The colour map represents the depth (m), relative to CD.

5.3. Comparison of numerical and field data

In this section, each 30-min period of the total 127 periods (between the 12th and the 14th of May 2010), was simulated by the model during 300 s. The characteristics (Hs, Ts) of the wave conditions defined for each period were based on the time analysis of the values measured in PT00 instrument. The numerical results were obtained for PT00, PT01 and PT02 positions.

The model results were then compared with data measured *in situ*, in order to evaluate the ability of the model to simulate real data. Hence, for PT00, PT01 and PT02 locations, it was compared numerical and measured data of:

- Significant wave height (Hs) and significant period (Ts), for the period comprised between the 12th and the 14th of May, 2010, for each 30-min period of the 127 periods simulated;
- Statistical parameters: bias (BIAS), root-mean-square error (RMSE) and agreement index (8) (*d* – Willmott *et al.* (1985)), given by:

$$d = 1 - \frac{\sum_{i=i}^{n} |y_i - x_i|^2}{\sum_{i=i}^{n} (|y_i - \bar{x}| + |x_i - \bar{x}|)^2} \tag{8}$$

where x_i are the field values (reference), y_i the numerical values, $\bar{x}$ the mean of field values and n the number of data values considered. The agreement index, *d*, varies from zero to one, where one represents the greatest agreement between numerical and field data.

- Fourier and Wavelet power spectra calculated for a single 30-min interval (chosen as an example), starting at 3:00, on the 13-05-2010. For this analysis only, the 30-min intervals were simulated during 1800 s (as opposed to the remaining analysis, were intervals were simulated only for 300 s, due to computational limitations), in order to allow a better spectral analysis, which would hardly be possible for 300-s simulations. The first 200 s of simulation and field data were excluded from this analysis, as the time considered for the model to attain its full performance.

With the horizontal velocity values acquired in the ECM position, it was compared numerical and measured data of:

- Maximum, minimum, mean and root-mean-square velocities, between the 12th and 14th of May, 2010, for both cross-shore and longshore components;
- For the above velocities, the same statistical parameters of BIAS, RMSE and *d*.

5.3.1. Free-surface displacement

5.3.1.1. Comparison of numerical and field values of Hs and Ts

Fig. 5 presents a comparison of numerical and field data values of Hs and Ts, for PT00, PT01, PT02 positions.

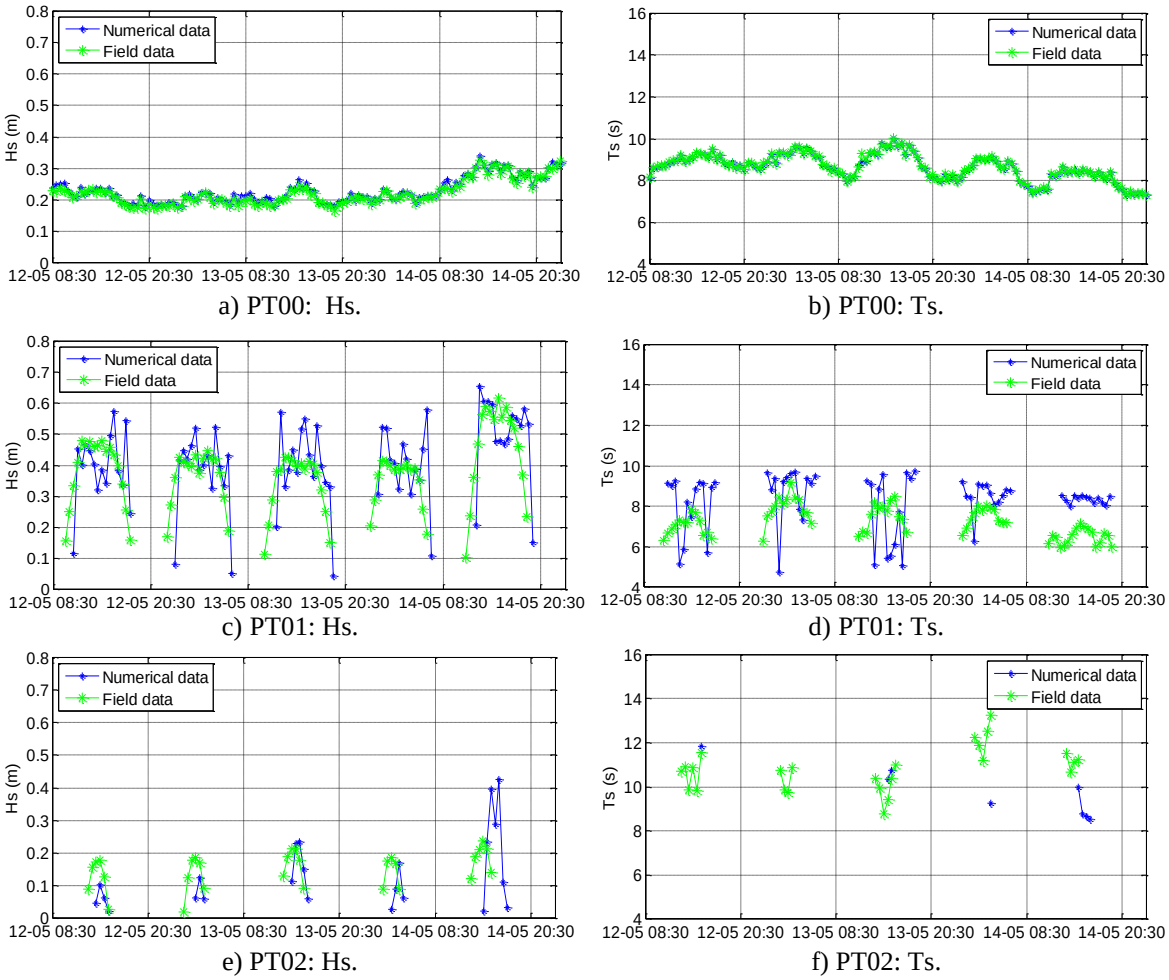

a) PT00: Hs. b) PT00: Ts.

c) PT01: Hs. d) PT01: Ts.

e) PT02: Hs. f) PT02: Ts.

Fig. 5 – Comparison of numerical (blue) and field (green) data for a) Hs (m) and b) Ts (s), at PT00 location, c) Hs (m) and d) Ts (s), at PT01 location and e) Hs (m) and f) Ts (s), at PT02 location.

For a more thorough analysis, Table 3 and Table 4 show the values of BIAS, RMSE and *d*, for both Hs and Ts, respectively, and for each instrument position.

Table 3 – Values of BIAS, RMSE and *d* calculated for Hs values, in PT00, PT01 and PT02 locations.

Instrument	BIAS (m)	RMSE (m)	*d*
PT00	0.007	0.009	1.00
PT01	0.023	0.126	0.93
PT02	0.126	0.105	0.84

Table 4 – Values of BIAS, RMSE and *d* calculated for Ts values, PT00, PT01 and PT02 locations.

Instrument	BIAS (s)	RMSE (s)	*d*
PT00	-0.006	0.025	1.00
PT01	0.912	1.891	0.93
PT02	-	-	-

In this analysis, the field and/or numerical values of Hs and Ts corresponding to 30-min, or 300-s, periods of low-tide, when the instruments were emerged, were not considered. Moreover, the statistical analysis of Ts values for PT02 position is not presented, since for this position there were too few representative and realistic values available to be considered. It is also important to note that the removal of unrealistic values from the samples, which becomes particularly relevant for PT01 and even more for PT02, will influence the calculations of the statistical parameters and will tend to mask their real values, especially in the case of the agreement index.

Comparing the numerical data with field data, for each instrument position, it is clear that:

PT00

- The numerical values simulate very closely the field data, with BIAS and RMSE as small as 0.007 and 0.009 m, respectively, for Hs, and -0.006 and 0.025 s for Ts. The agreement index, with a value of approximately 1.00, further points out the ability of the model to simulate, for the position of PT00 (the source of the waves in the model), both the trend and absolute values of Hs and Ts.
- Observing the Hs trend, it is also evident that during the period of the campaign the wave climate was fairly mild, mostly a result of local wind forcing, with small wave heights and periods, becoming slightly more energetic by the end of the period (14th May 2010), when the maximum and minimum values, respectively of Hs and Ts, were registered.
- It is further noticeable an oscillation of the measured Ts values following cycles of about 12 h, approximately between 8 s and 10 s.

PT01

- The model simulates the general trend and magnitude of Hs field values. It also simulates the low-tide discontinuities present in the field data, concomitant with the low-tide periods, both for Hs and Ts, which justifies the fairly high agreement index of approximately 0.93, for both Hs and Ts.
- It is clear a tendency of overestimation of the field values of Hs, denounced by the values of BIAS and RMSE, respectively 0.023 and 0.126 m. Despite the BIAS and RMSE of 0.912 and 1.891 s, calculated for Ts, point to a general tendency of overestimation of the field data, a great variation between consecutive numerical values of Ts leads to punctual over and underestimations of the field values, sometimes greater than 1 s. The variation of numerical values between 30-min intervals is also present for Hs, particularly during high-tides, but is less relevant.

PT02

- For this position, long periods of discontinuity, associated with the emersion of the instrument during low-tide, are present in both field and numerical data. Hence, few values are available for establishing comparisons, which limits a more thorough analysis.

Especially for Ts numerical values, the model is only capable of simulating very few 30-min intervals, which impedes a meaningful calculation of the statistical parameters.

- Nevertheless, the model is still fairly able of representing the general trend of the field values of Hs, which is corroborated by an agreement index of 0.84 and BIAS and RMSE of 0.126 and 0.105 m, respectively.

From a general perspective, the model is able of simulating the trends and orders of magnitude of the field data, particularly for Hs values. For Ts values, the absolute differences are greater.

For both PT00 and PT01 instruments positions, the numerical results obtained are quite promising, which points out the ability of the model to simulate wave propagation towards the shore, particularly before wave breaking. For locations higher up the beach profile, where the waves are expected to be already broken, the model reveals a greater difficulty in simulating field data.

The differences between numerical and field data can be a consequence of:

- The directions of numerical incident waves being always considered perpendicular to the coast (which aggravates wave conditions in the sensors near the shoreline), and not corresponding to the real directions of the waves that effectively arrived to shore in Cornélia beach, during the period of the campaign. This limitation was mostly an unavoidable consequence of the fact that the wave direction was not measured during the campaign.
- Limitations inherent to the model. Particularly, it is important to underline that the application of the model to bottom slopes of about 1/6 can be critical, since its fundamental equations are integrated assuming mild-sloping bottoms. Furthermore, phenomena such as wave breaking are included in the model through the addition, to the original equations, of a turbulent viscosity term, which depends on a set of parameters, related to the onset, duration and cessation of breaking events that should be calibrated for each single case study and wave condition imposed. These parameters, herein considered constant for all the 127 different incident wave conditions, should, for greater accuracy, be individually calibrated.

5.3.1.2. Spectral analysis of a 30-min interval

Fig. 6 and Fig. 7 show a spectral analysis of numerical and field data, for a single 30-min interval, for PT00, PT01 and PT02 positions, using two different methods: Fourier and Wavelet (Moura, 2010), respectively. These results allow the investigation of the ability of the model to simulate nonlinear characteristics of the waves, as they propagate, evidencing both the energy density distribution by frequencies (Fourier method) and the frequency distribution of the energy along the measuring time period (Wavelet method). It should be noted, however, that slight shifts in the exact position of the instruments in the model grid (along x and/or y) may have a significant influence on the spectral results simulated by the model, which can justify some of the differences between field and simulated data.

It is also important to note that the model was forced with monochromatic waves, and hence a dispersion of the energy to multiple frequencies is less expected than it is for field data, which is originated by irregular wave spectra. This is particularly evident for the instrument further offshore and thus closer to the wave-source, since nonlinear effects associated with wave shoaling and wave

breaking can also cause this energy dispersion to multiple frequencies for the instruments positioned closer to the shore.

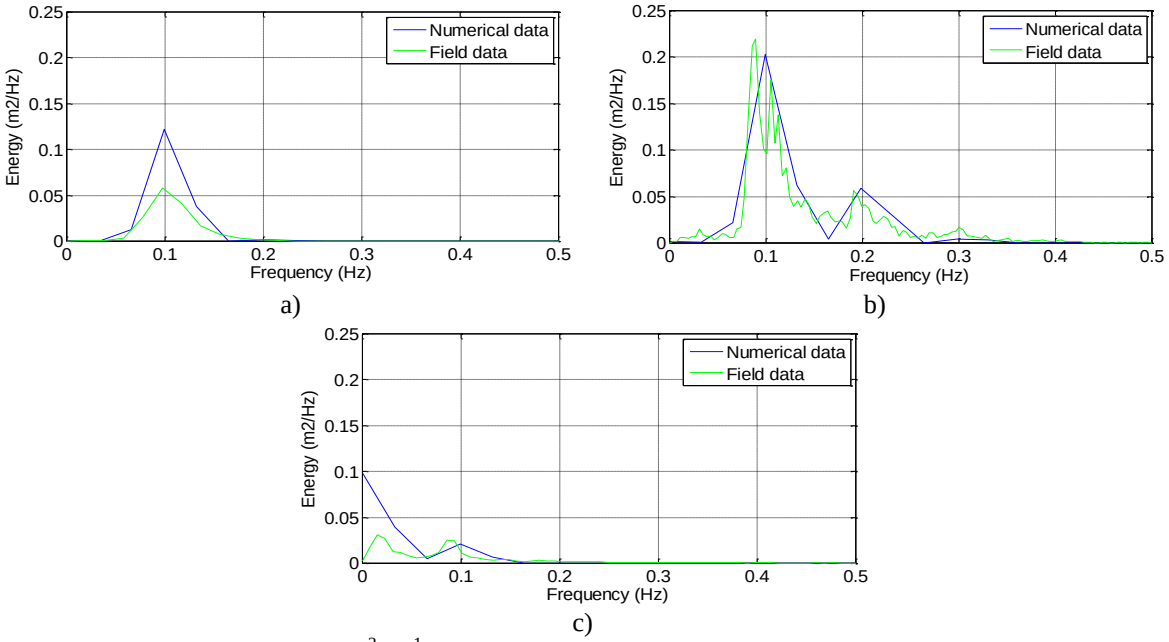

Fig. 6 – Fourier energy spectra (m^2Hz^{-1}) field data versus numerical results in a) PT00, b) PT01 and c) PT02 locations. The chosen 30-min interval starts at 3:00 on the 13-05-2010.

Fourier spectra reveal that the higher-energy frequencies present in the field data are well simulated by the model. Despite the nonlinear energy transfers between waves of different frequencies, expected to happen in the case of the two sensors further inshore, PT01 (Fig. 6b) and PT02 (Fig. 6c), not being simulated by the model, the model is able of representing the two main frequency peaks. In PT01, the peak correspondent to the 10-s period, also evident in PT00 (Fig. 6a), is present, and a new peak, of lower energy and period, appears. In the case of PT02, Fourier spectra are clearly different from the previously observed in the other sensors. There is still some energy associated with the 10-s period, but there is a transfer of energy to longer periods, which denounces the occurrence of more significant nonlinear phenomena.

Wavelet spectra permit a more thorough analysis of the distribution of energy to the main frequencies, since they allow the evaluation of the importance of each frequency along the analyzed 30-min interval.

Firstly, it is evident that in PT01 (Fig. 7c and Fig. 7d) the waves have a greater energy than in PT00 (Fig. 7a and Fig. 7b) and PT02 (Fig. 7e and Fig. 7f) position; this is particularly evidenced by the energy scale of each figure. PT02 has the less energetic spectra, by an order of magnitude. This is concordant with waves breaking in the vicinity of PT01, and hence dissipating most of their energy before reaching PT02 position.

In the situation of PT00 field data, a range of periods with higher associated energy (approximately between 7 and 11 s) can be identified, as well as the higher-energy time instants of the study interval, which occur around the 400 and the 1500 s instants (Fig. 7a). Naturally, due to the monochromatic forcing of the model, the wavelet spectrum obtained for the numerical data, in PT00 (Fig. 7b), exhibits a more confined range of energy frequencies, typical of the regular wave conditions input. For PT01 and PT02 (Fig. 7d and Fig. 7f) the model identifies the main range of periods present, of about 10 s, and represents relatively well the presence of a group of

higher-frequencies (0.2 Hz), for PT01, and lower-frequencies (0.05 Hz) for PT02, with less associated energy.

However, the model is still limited on the simulation of energy dispersion to higher and lower frequencies than the higher-energy frequencies, which acquires a particular relevance for the instruments closer to shore.

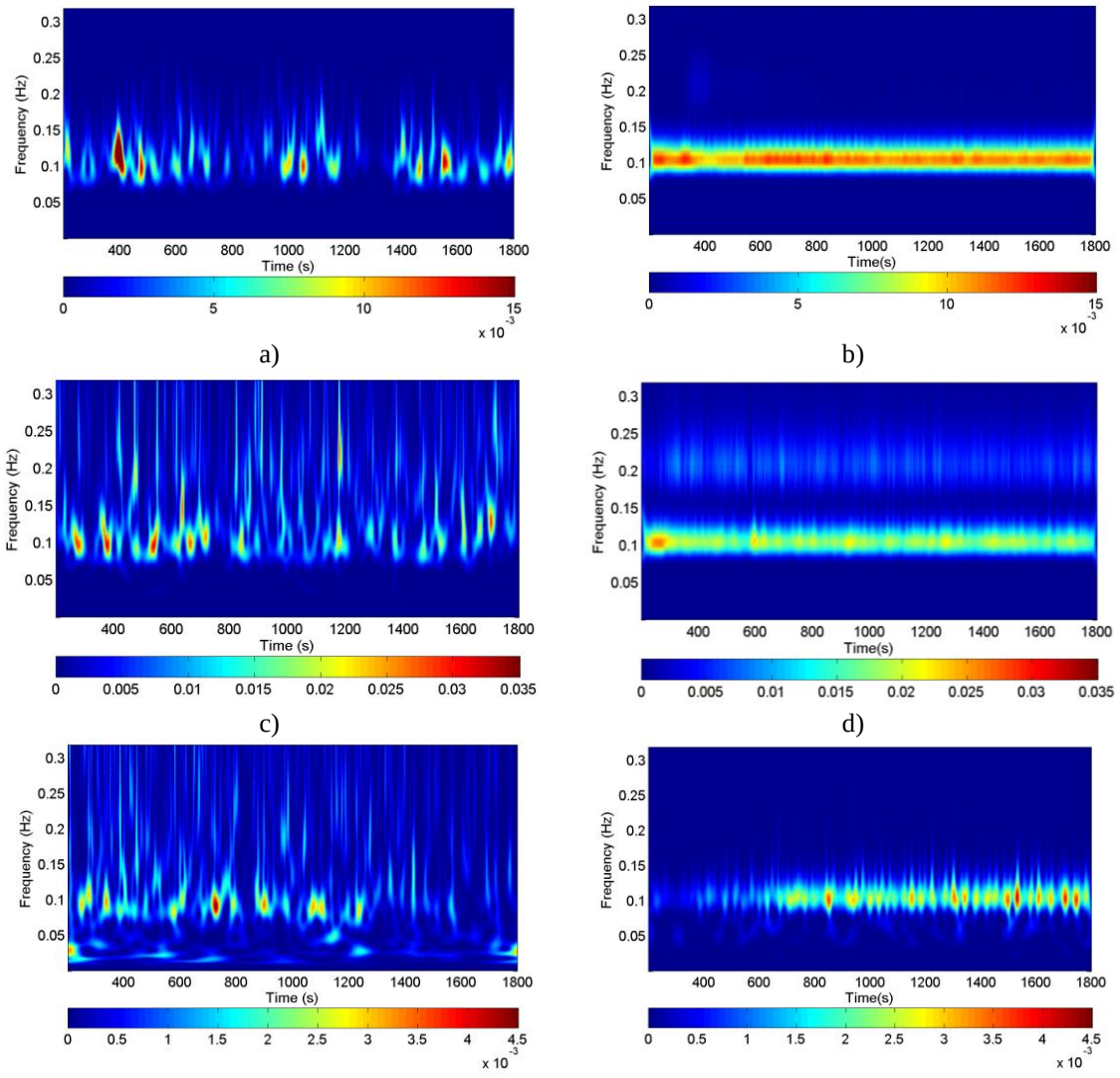

Fig. 7 – Wavelet energy spectra (m^2Hz^{-1}) of field data (left column) versus numerical results (right column) for a) and b) PT00, c) and d) PT01 and e) and f) PT02 locations. The chosen 30-min interval starts at 3:00 on the 13-05-2010.

5.3.2. Horizontal velocity – comparison of velocity numerical and field values

Fig. 8 and Fig. 9 present a comparison between field and numerical data for maximum, minimum, mean and root-mean square cross-shore (U) and longshore (V) components of the horizontal velocity, respectively.

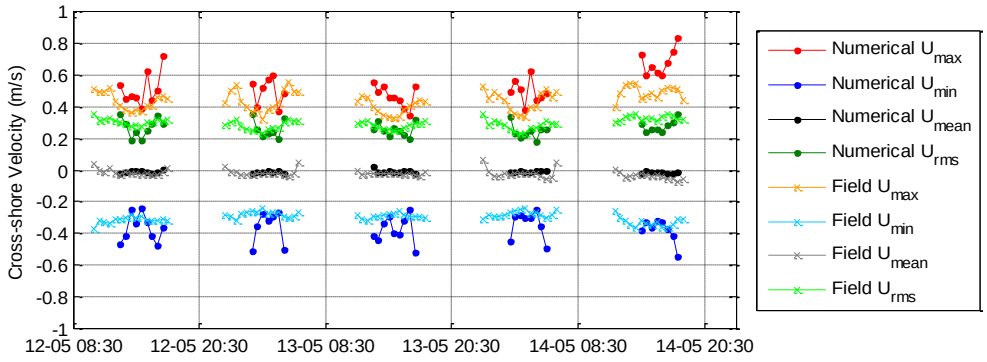

Fig. 8 – Comparison of numerical (dots) and field (crosses) maximum, minimum, mean and root-mean-square velocities (ms^{-1}) of the cross-shore (U) component.

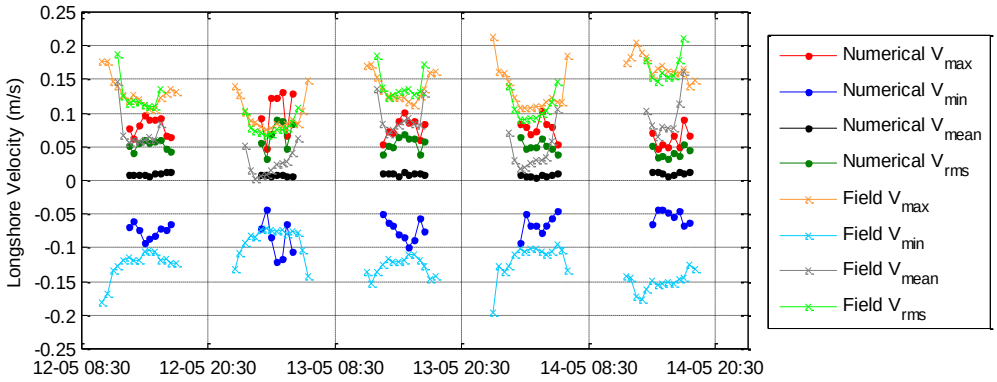

Fig. 9 – Comparison of numerical (dots) and field (crosses) maximum, minimum, mean and root-mean-square velocities (ms^{-1}) of the longshore (V) component.

Also for the horizontal velocity, the values of BIAS, RMSE and *d* were calculated, and are present on Table 5 and Table 6, respectively for cross-shore and longshore components.

Table 5 – Values of BIAS, RMSE and *d* calculated for maximum, minimum, mean and root-mean-square velocities of the U component.

Velocity	BIAS (ms^{-1})	RMSE (ms^{-1})	*d*
Umax	0.186	0.322	0.51
Umin	-0.119	0.169	0.49
Um	0.010	0.036	0.71
Urms	0.006	0.085	0.94

Table 6 – Values of BIAS, RMSE and *d* calculated for maximum, minimum, mean and root-mean-square velocities of the V component.

Velocity	BIAS (ms^{-1})	RMSE (ms^{-1})	*d*
Vmax	-0.037	0.055	0.90
Vmin	0.057	0.072	0.88
Vm	0.072	0.083	0.73
Vrms	-0.079	0.097	0.84

Analyzing Fig. 8, Fig. 9, Table 5 and Table 6, it is possible to draw some conclusions on the variations of maximum, minimum, mean and root-mean-square velocities for both U and V components measured by the ECM and simulated by the model.

It is important to note that the field values of velocity are measured near the surface, and the numerical values are calculated at a $z_1 = -0.531h$ depth, which is located approximately at water-column mid-depth. This could help explaining some of the differences between field and numerical data. Also, the values of velocity measured and simulated during lower water-level periods tend to present unrealistically higher values, as the ECM is emerged. These values were excluded from analysis (the same number for both components and the same number for both field and numerical data in the calculation of the statistical parameters), although some values in the beginning and the end of each of the five intervals considered for analysis are still biased due to the progressive emersion of the ECM. Hence, the calculation of the values of BIAS, RMSE and *d* implied the exclusion of several values, which reduced the size of the sample and tends to mask the real values of these statistical parameters, which should thus be considered with care.

Although the model generally overestimates and underestimates, respectively for U and V components, the absolute values of maximum, minimum, mean and root-mean-square velocities, field and numerical data still present a similar behaviour:

- Of the two components, the cross-shore has higher amplitude between maximum and minimum velocities, deviating from its mean value, of about 0.00 ms^{-1}, to reach maximums of roughly 0.50 ms^{-1}, in the case of field data, slightly higher for numerical data, and minimums of about -0.30 ms^{-1}, also slightly lower for numerical data.
- The cross-shore component reaches higher absolute velocities in the way of the wave propagation (positive), which evidences the presence of nonlinear waves, with cnoidal or 2nd order Stokes shapes, characterized by higher and shorter crests and lower and longer troughs.
- The longshore component has smaller amplitude between maximum and minimum velocities and a minor absolute maximum value, significantly lower than the one of the cross-shore component, hardly reaching 0.20 ms^{-1} for both Vmax and Vmin. This is a consequence of the low obliquity of wave propagation towards the coast. In the inverse case, of high obliquity ($|\theta|>45°$), it would be expected Vmax and Vmin to be superior to Umax and Umin. A visual observation of wave conditions during the measurement period warranted the arrival of waves to the coast from the SW-NW quadrant. The exact value of this direction can be determined following the methodology of Taveira (2010), that performs an ECM-coordinates rotation, in order to align the wave propagation with the *x*-axis.
- Root-mean-square velocity, which is implicitly an absolute velocity, exhibits positive values only. Again due to the low-obliquity of the incident waves, the values of Urms, which reach over 0.30 ms^{-1}, are throughout the period greater than Vrms values, of about 0.05 ms^{-1}, in the case of numerical data, and around 0.15 ms^{-1}, in the case of field data.
- The mean velocity of the longshore component exhibits a value slightly greater than zero (up to 0.10 ms^{-1}), particularly in the field data, pointing to a predominance of a NW-SE velocity direction, which denounces the present of a longshore drift running along this direction, resulting from the obliquity of waves propagating from the NW-SW quadrant. It is also evident an increase of Vmean absolute values during the periods of measurement

with lower water-level, when the ECM was located within the surf zone, while for measurements during high-tide the measured current is much weaker, since the sensor would be in a location before the surf zone, thus in the presence of a weaker current.

- Cross-shore mean velocity remains mostly around -0.02 to -0.03 ms^{-1}, in field data, and -0.01 to -0.02 ms^{-1}, in numerical data, evidencing the presence of a weak undertow. During the 30-min intervals immediately before and after the periods not considered in the analysis, measured Umean is closer to zero or positive (directed shorewards). This is a result of the ECM being relatively close to the surface during those measurements, due to the lower water depth and hence measuring not the undertow, but a current similar to the Stokes drift. In the case of numerical data, the measuring depth is always at about half-way down the water column, so this oscillation between surface currents and undertow, evident in the ECM data, is less relevant.

Comparing numerical and field data, it is evident that:

- For both U and V components, the BIAS and RMSE values close to zero point to a good model performance, in the simulation of velocity for PT01 location. It is however clear, from Fig. 8 and Fig. 9, the greater difficulty of the model to conveniently simulate the conditions observed during the 30-min intervals of the last tide cycle, particularly for V component, in which an excessive deviation between measured and simulated data is noticeable.
- The order of magnitude of field data is well represented, but the model seems less able to describe the general trend. Numerical data (maximum, minimum, mean and root-mean-square velocities) show greater oscillation between consecutive 30-min intervals than field data, which justifies the relatively low values of the agreement index.
- The over- and underestimation of, respectively, U and V field data, are most likely related to the wave propagation direction: the model was forced with perpendicular wave directions to the coast, which induces greater values of U, and smaller values of V, contrariwise to the real direction of propagation in the field, where the obliquity of the waves propagating to shore will tend to result in a weaker-than-simulated U component and stronger-than-simulated V component.

6. SIMULATION OF GROIN IMPACT

6.1. Introduction

In this section the model was applied to study groin impact on significant wave height and horizontal velocity near the shore. Different groin lengths and orientations relatively to the coast, and different incident wave heights and sea-surface levels were tested.

The scenarios

Several scenarios were considered, aiming the understanding of the influence of groin length and orientation (relatively to the direction perpendicular to the shoreline) and of incident wave height and sea-surface level (analogously to tide level), on the significant wave height and horizontal velocity near the shore. The characteristics of the scenarios correspond to the:

- Variation of the groin lengths: L=200 m, L=250 m, L=300 m and L=400 m;

- Variation of the groin orientations: $\phi = 10°$, $\phi = 15°$, $\phi = 25°$ and $\phi = 30°$;
- Variation of the incident-waves significant height: Hs=1.0 m, Hs=1.5 m, Hs=2.0 m and Hs=3.0 m;
- Variation of the sea-surface level: SSL=0.50 m, SSL=0.75 m, SSL=1.50 m and SSL=2.40 m.

All the scenarios are compared with a so called **control-scenario** with a groin defined by L=200 m and ϕ=10° and considering the incident wave with Hs=1.0 m and SSL=0.50 m;

This choice of scenarios intended to approach a wide range of possibilities often considered in real situations and to analyze the influence of four of the most important parameters to be considered when a groin has to be built. However, it was also constrained by model limitations, such as the difficulty (or even impossibility) of the model to simulate scenarios where wave breaking would occur too close to the head of the groin. In such cases, the model would crash, most likely due to the abrupt change in bathymetry caused by the imposition of the groin to the original bathymetry of the domain. Wave heights, too high or too small, were also a problem for the model to simulate wave breaking events.

The groins

For each simulation, the landward groin end was positioned the furthest away possible from the reflective boundaries (approximately at *x*=890 m and *y*=440 m, slightly changing for each scenario). Its length, L, was measured seawards from the shoreline, and its shoreward tip was extended to the right boundary of the domain. All the groins were designed to have a width, W, of 6 m on the top, located at 5 m above chart datum, h, and a side-slope of ½ (V/H) (Fig. 10).

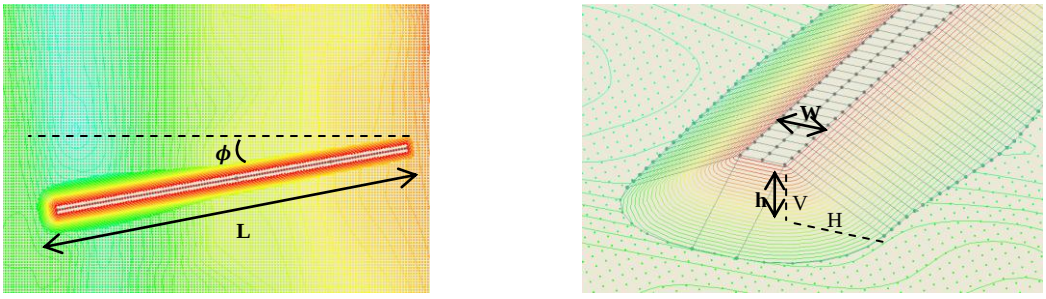

a) b)

Fig. 10 – Groin characteristics: a) Length and orientation and b) Height, width and side-slope.

The transects

To evaluate groin impact in each scenario, 9 transects, both along *x* and *y* directions, were chosen (Fig. 11). The *x*-transects were comprised between *x*=400 m and *x*=800 m, with a spacing of 50 m, and the *y*-transects between *y*=200 m and *y*=600 m, with the same spacing of 50 m. The choice of these transects was intended to cover the area of the domain expected to be most affected by the groin.

The analysis

Firstly, for each scenario, the significant wave height and the mean breaking locations across the domain were calculated for the entire domain. The domain colour maps for these two variables are presented, mostly to help the subsequent analysis performed for the transects and to provide a general view of the different scenarios (view, for e.g., Fig. 12).

Afterwards, and for each grid point of the transects, the percentage relative difference between the considered scenario and the control scenario was calculated, and differences greater than a pre-established value (to be specified later, for each parameter – 5%, 7.5% or 10%) were considered significant for the ensuing analysis. The value of the percentage of the difference defined for each parameter (5%, 7.5% or 10%) was chosen to be the lower limit from below which the differences become too spread over the entire domain to have any significance. These differences between each scenario and the control scenario were calculated for Hs and U (Umax, Umin and Umean) and V (Vmax, Vmin and Vmean) components of horizontal velocity, in the case of the control runs, and only Hs for the other runs.

The grid points along the transects where the differences were considered significant were evidenced in the domain (by black stretches – lines constituted by grid points marked in black – view Fig. 11 for schematic e.g.), and the extension (length) of this black stretches was calculated for each transect. From this, the total length of the stretches for all the 9 transects in each direction was determined.

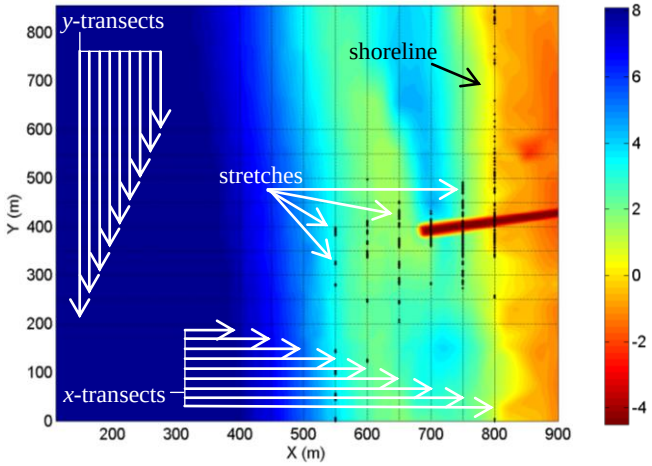

Fig. 11 – Schematic representation of the transects and stretches mentioned in the analysis. The shoreline corresponds to the zero-depth colour of the colour map (m).

Besides evaluating the length of stretches (where differences were considered significant), the absolute value of mean change was also evaluated (for e.g., view Fig. 13d and Fig. 13f). This mean change is a spatial-average, obtained for each transect, from the value of the Hs (or Umax, Umin, Umean, Vmax, Vmin, Vmean) difference between both scenarios, in each grid point of the transect.

The calculation of Hs implies a time-average of the highest 1/3 of wave heights simulated by the model along the 300 s of simulation. Umean and Vmean are simple time-averages respectively of U and V components of the horizontal velocity, in each grid point. However, it is important to note that U and V can have both positive and negative values, depending on which direction the velocity vector points to, and thus the signs of Umean and Vmean values reflect the mean direction of cross-shore and longshore components. In turn, Umax and Umin and Vmax and Vmin are the mean maximum and mean minimum values, respectively, and for each of the velocity components, registered during the total period of 300 s. These mean of maxima and mean of minima are calculated using the zero-crossing method. The same methodology was applied for both *x*- and *y*-directions transects.

When observing the plots, some important issues should be considered:

- The domain output by the model does not match the exact domain considered: along the *x*-direction, the considered domain was extracted from the output domain for values of *x*

between 110 and 1010 m. This was done in order to exclude from visualization the boundary-layer part of the output domain, in both right and left boundaries. The extent of these boundary layers was observed to vary from one scenario to another, reaching variations of about 100 m or more, determined by the model. Nevertheless, and for simplification purposes, the extracted domain was for all scenarios considered the same.

- Together with the boundary layers, also the *x* and *y* positions and the spacing of the grid points varied from one scenario to another. Hence, for each scenario, the values of Hs (and velocities) had to be interpolated to a regular 900x858 m grid (original dimensions of the domain input to the model), before the transects were defined, in order to establish a standard procedure and comparable data for analysis.
- Due to model limitations (such as its spatial resolution), some values of Hs (and velocities) were calculated for grid points which were above the sea-surface level. Hence, these values affect the calculations of the length of the stretches where differences were considered significant and consequently the mean change values, and are erroneously marked with black on the colour maps. Despite the minor effect of these errors on the length of the black stretches and on mean change values, care must be taken when interpreting the colour maps, in order to not consider the stretches of the transects above de sea-surface level.
- The values of mean difference along the transects represented on the mean change plots are absolute values and should thus be considered with care. For the percentage relative difference, the colour maps should be analysed. This is particularly relevant, for e.g., in the *x*-transects closer to the shoreline, since the waves there, already broken, have smaller Hs, and a smaller absolute Hs difference between scenarios, but eventually a greater relative difference.
- For a question of simplicity, the side of the groin closer to the upper boundary of the domain will be designated as its upper side or updrift side, and the side closer to the lower boundary will be called the lee-side, lower side or downdrift side.

6.2. Control runs

Firstly, and to understand the groin impact on a beach, two simulations were run:

- No groin – The bathymetry of the domain did not include any groin, the incident significant wave height considered was 1.0 m and the sea-surface level was assumed to be 0.50 m.
- Control Groin – A 200 m-long groin was added to the bathymetry of the domain, 10º rotated to the lower side of the shoreline-perpendicular. The incident wave and sea-surface level were considered the same as in the previous simulation.

The relative Hs and velocities differences between both runs were considered significant when greater than 10%.

Fig. 12 presents the domain colour maps of Hs (Fig. 12a and Fig. 12b) and wave breaking (Fig. 12c and Fig. 12d), for both no-groin and control-groin runs. The colour bar present in the Hs colour maps indicates the values of Hs (m). The brownish area represents land, i.e., the area of the domain that, during the 300 s of each simulation is, in average, above the sea-surface level. For the breaking colour maps, the dark blue regions are regions where breaking never occurs during the 300 s of each run. Apart from the dark blue regions, the warmer the colours represented, the more frequently, in average over the 300 s, wave breaking occurs in those regions.

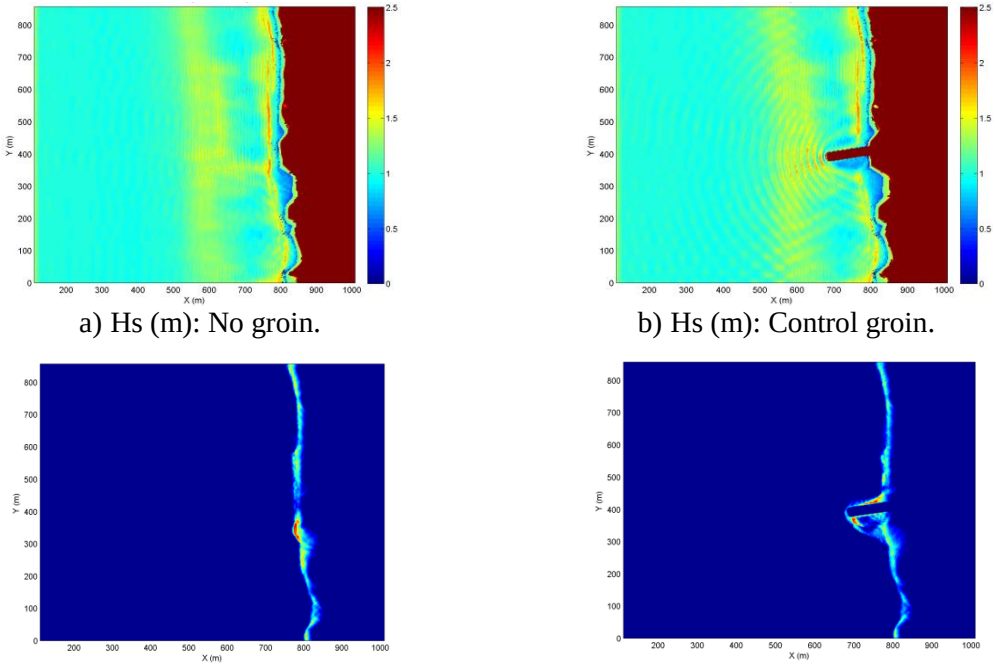

a) Hs (m): No groin. b) Hs (m): Control groin.

c) Wave breaking: No groin. d) Wave breaking: Control groin.

Fig. 12 – Colour maps of Hs (top line) and wave breaking locations (bottom line) in the domain, for no-groin run, respectively a) and c), and control-groin run, respectively b) and d).

From Fig. 12, it is possible to verify that wave height increases near the head of the groin, and hence waves break adjacent to this point, towards the lee-side of the groin. The presence of the groin affects most of the domain, generating a diffraction effect and a shadow-zone close to shore, on the lee-side of the groin, where the waves are already broken and Hs is small. In the upper-side of the groin, reflection is the most important phenomenon.

Fig. 13a and Fig. 13b colour maps represent the depth of the domain. In Fig. 13a and Fig. 13b, the grid points of the *x*- and *y*-transects, respectively, where the percentage relative Hs differences between control-groin and no-groin runs were greater than 10% were evidenced in the domain (marked with black stretches, and henceforth named **stretches of Hs change**).

Fig. 13c and Fig. 13e plots show the sum of all the grid points marked with black (total length of the various stretches, henceforth named **length of groin impact**), in each transect, in Fig. 13a and Fig. 13b, respectively. Fig. 13d and Fig. 13f plots present the mean (along each transect) of the Hs difference (in each grid point of that transect) between control-groin and no-groin runs, for *x*- and *y*-transects, respectively (henceforth named **mean change**). For these four figures, the continuous black lines marked along the x=0 (and y=0) axis represent, approximately, the positions along x (and along y) that, at some point along y (and x) are crossed by the groin. Analogously, for other scenarios, different lines with different dashes will represent the different groins, when necessary.

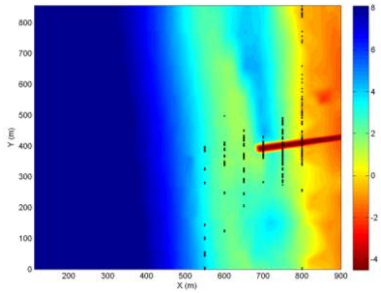

a) Stretches of significant Hs differences along *x*-transects.

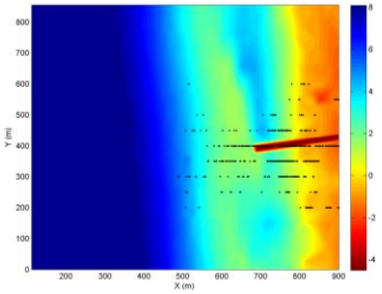

b) Stretches of significant Hs differences along *y*-transects.

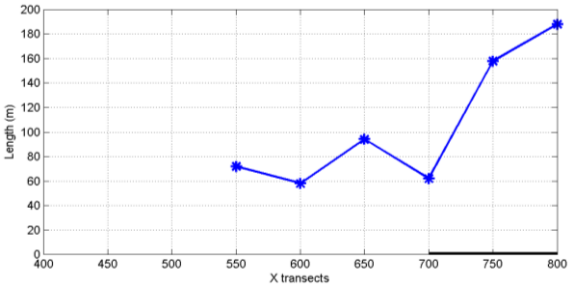

c) Length (m) of groin impact along *x*-transects.

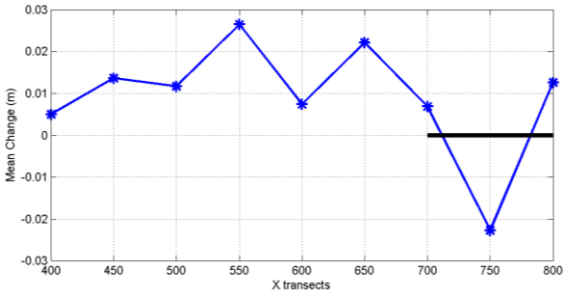

d) Mean change (m) along *x*-transects.

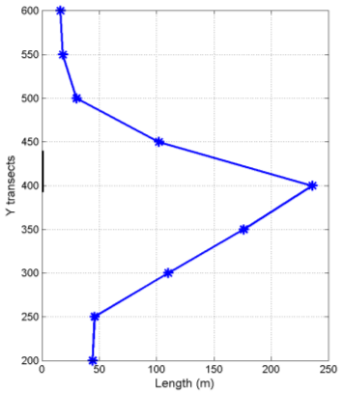

e) Length (m) of groin impact along *y*-transects.

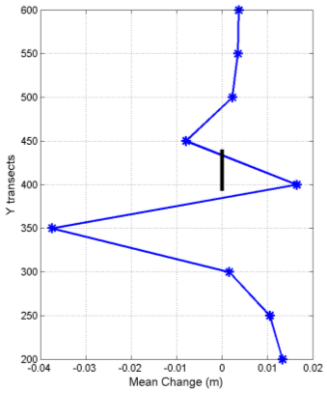

f) Mean change (m) along *y*-transects.

Fig. 13 – Impact of the groin in Hs: a) and b) Stretches of the transects where the Hs differences between control-groin and no-groin runs are greater than 10%, respectively along *x* and *y* transects. c) and e) Length of the referred stretches, for each transect, respectively along *x* and *y*. d) and f) Mean Hs change (differences between control-groin and no-groin runs), for each transect, respectively along *x* and *y*.

Some aspects of the impact of the groin can be noticed in Fig. 13. Percentage relative differences in significant wave height greater than 10% are more important close to the groin (within about 100 m) and on its lee-side (where the stretches of Hs significant differences have greater lengths). For the region further offshore than the submerged bar, hardly any differences of Hs reach 10%. Stretches of Hs significant differences extend longer along the *y*-direction in the region further inshore than the head of the groin. Along the *x*-direction, the stretches extend mostly in the line of the groin and in a vicinity of less than 100 m.

In the area further outside the tip of the groin, Hs increases, mostly near the head, and decreases in the inner (the groin) region. Also in the shadow-zone of the structure, in its lee-side, the wave height diminishes. Although more transects account for a wave height increase, this change is less important and more localized in the vicinity of the groin, since it extends along

shorter stretches of the transects than the wave height decrease, which affects a wider area of depths shallower than the head of the groin.

Hence, the tendency seems to be of a general Hs decrease, accompanied of a Hs local increase, particularly focused further out and near the head of the groin. This is a result of the bathymetry change imparted by the groin: near its head, the end-slope, extending downwards to the sea-bottom, provides a region of bathymetry shallower than the original, where waves will shoal, increase their height and eventually break. This is also valid for the upper (in the domain) side-slope of the groin, whereas in the lower (in the domain) side of the groin, which becomes a sheltered zone, due to the diffraction effect that results from groin orientation, the waves break further offshore than before the addition of the groin.

Fig. 14 and Fig. 15, respectively, present an analysis of U and V components of horizontal velocity, analogous to the analysis performed on Fig. 13, for Hs.

These figures show the impact of the groin in both horizontal velocity components. Significant differences in Umax and Umin extend in the transects along similar lengths and happen mostly in the close vicinity of the groin. However, along the *x*-direction, particularly in front of the groin tip, a decrease of Umin is associated with an increase of Umax. Along the *y*-direction, the greater differences are observed within a 50 m-vicinity of the groin. Umax diminishes in every transect except where the groin is located, where it increases significantly, contrariwise to Umin, which tends to weaken near the groin, and increase further away from it. Umean hardly changes for depths further out than the head of the groin and for the transects more than 50 m to both sides of it. Conversely, Umean suffers the most significant mean change resulting from the groin impact, for the inner-groin transects, and the transect that crosses the groin: for these transects, Umean, initially negative (directed seawards), becomes significantly positive (directed shorewards), justifying the greater values of mean change registered.

The longshore component of velocity exhibits substantial changes, when the groin is added to the domain. Both absolute Vmax and Vmin increase about equally, and the differences of V between control-groin and no-groin runs spread across almost the entire domain. Along the *x*-direction, a decrease of mean change is noticeable, as transects further offshore are considered. Along the *y*-direction, very little mean change is evident for transects more than 50 m away from the groin, particularly to its upper-side.

The presence of the groin results in greater significant wave heights and frequency of breaking events near its head, where before no breaking would occur. Associated with these events, there is an increase in the cross-shore velocity towards the shore, near the groin and in the breaking region, and an increase in the seaward direction, in regions further away from the groin, as the water must return offshore, after the wave breaking. Since the model simulates the velocity at mid-depth of the water column, without the groin, the most relevant cross-shore velocity close to shore is a weak undertow, so usually U is most frequently directed offshore than towards the coast, although higher absolute values are registered in the direction of the coast, most likely associated with wave breaking events. The groin introduces in the domain more regions where breaking events are most relevant, particularly near its tip, and hence cross-shore velocity towards the coast increases in this region, and further away the weak undertow, directed offshore, persists (Fig. 16). In areas where no breaking events happen, since the model only simulates the velocity field associated with the propagation of the waves (which were input to the model propagating perpendicularly to the shore), mean velocity is almost zero, as the water particles oscillate back and forth as the waves pass by.

Since the waves propagate perpendicularly to the shore, the initial velocity field is mostly along the cross-shore direction. The groin also changes this aspect, particularly by inducing more

breaking events and phenomena such as diffraction and reflection, which justifies the significant differences in the V component of velocity that spread to almost the entire domain.

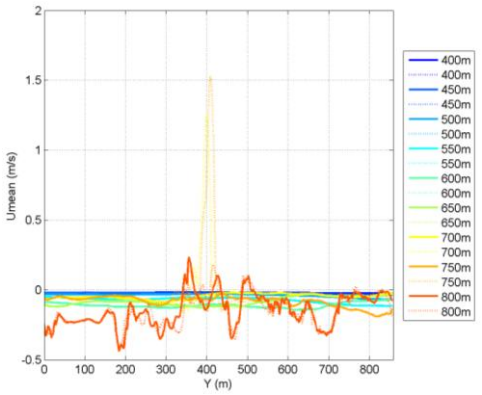

a) Umean (ms^{-1}) for no-groin run (full line) and control-groin run (dotted line), along the *x*-transects.

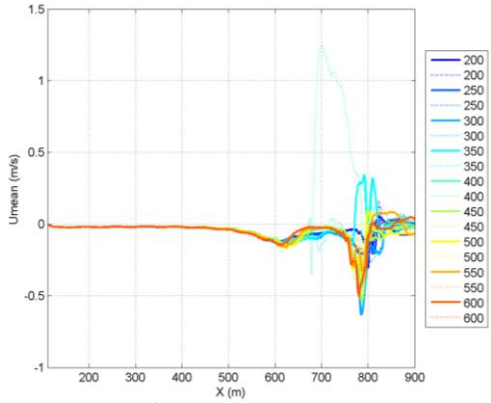

b) Umean (ms^{-1}) for no-groin run (full line) and control-groin run (dotted line), along the *y*-transects.

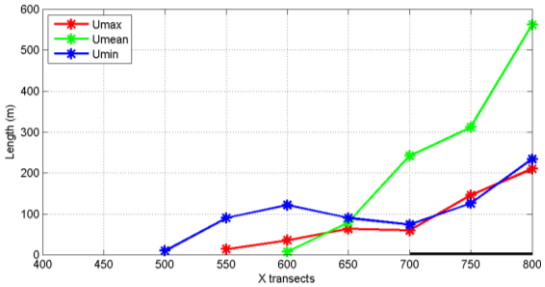

c) Length (m) of groin impact along *x*-transects.

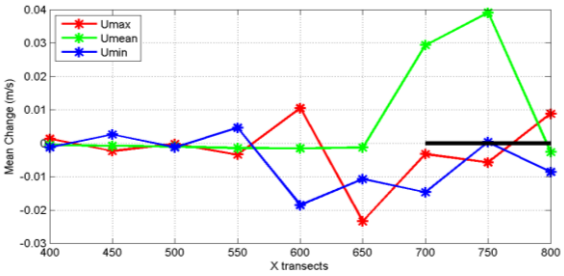

d) Mean change (ms^{-1}) along *x*-transects.

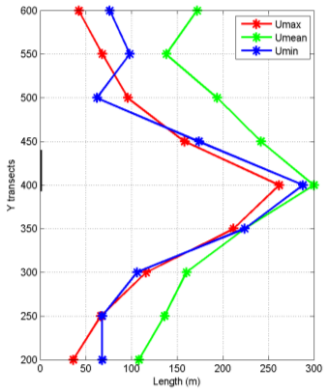

e) Length (m) of groin impact along *y*-transects.

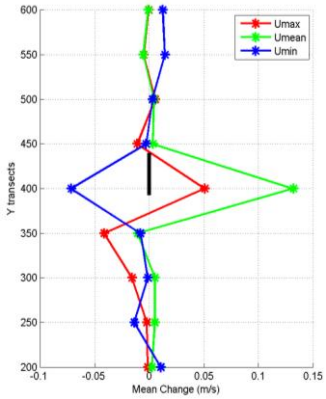

f) Mean change (ms^{-1}) along *y*-transects.

Fig. 14 – Impact of the groin in the cross-shore component of horizontal velocity: a) and b) Umean velocity, respectively along *x* and *y* transects. Dotted lines represent Umean for control-groin run, in each transect. c) and e) Length of the stretches of the transects where the Umax, Umean and Umin differences between control-groin and no-groin runs are greater than 10%, respectively along *x* and *y* transects. d) and f) Mean Umax, Umean and Umin change (differences between control-groin and no-groin runs), for each transect, respectively along *x* and *y*.

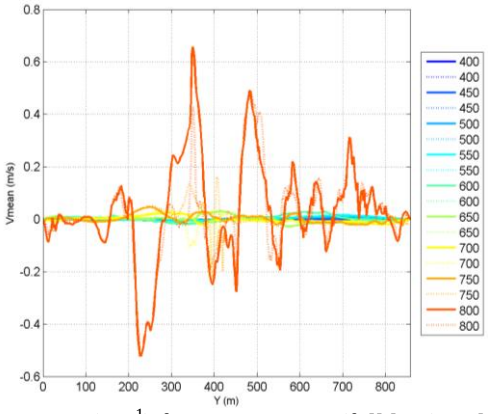

a) Vmean (ms^{-1}) for no-groin run (full line) and control-groin run (dotted line), along the *x*-transects.

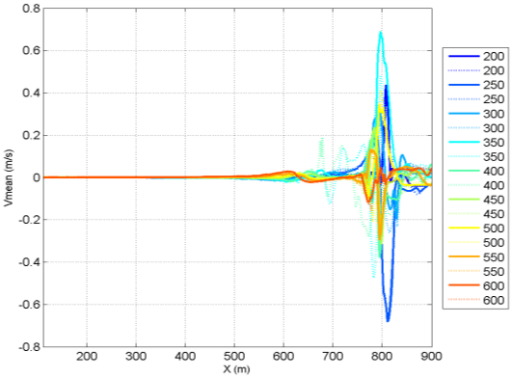

b) Vmean (ms^{-1}) for no-groin run (full line) and control-groin run (dotted line), along the *y*-transects.

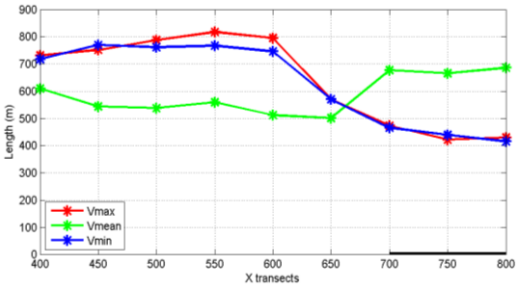

c) Length (m) of groin impact along *x*-transects.

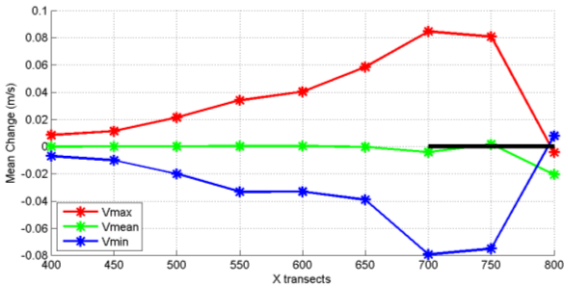

d) Mean change (ms^{-1}) along *x*-transects.

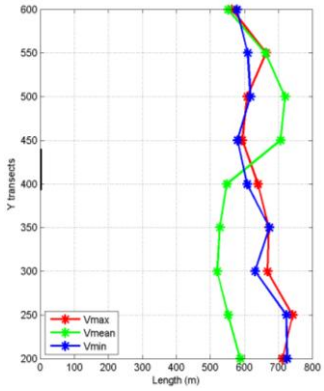

e) Length (m) of groin impact along *y*-transects.

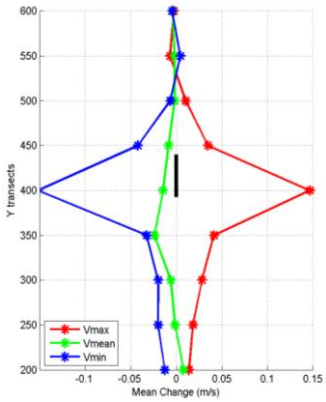

f) Mean change (ms^{-1}) along *y*-transects.

Fig. 15 – Impact of the groin in the longshore component of horizontal velocity: a) and b) Vmean velocity, respectively along *x* and *y* transects. Full and dotted lines represent Vmean for no groin and control-groin runs, in each transect. c) and e) Length of the stretches of the transects where the Vmax, Vmean and Vmin differences between control-groin and no-groin runs are greater than 10%, respectively along *x* and *y* transects. d) and f) Mean Vmax, Vmean and Vmin change (differences between control-groin and no-groin runs), for each transect, respectively along *x* and *y*.

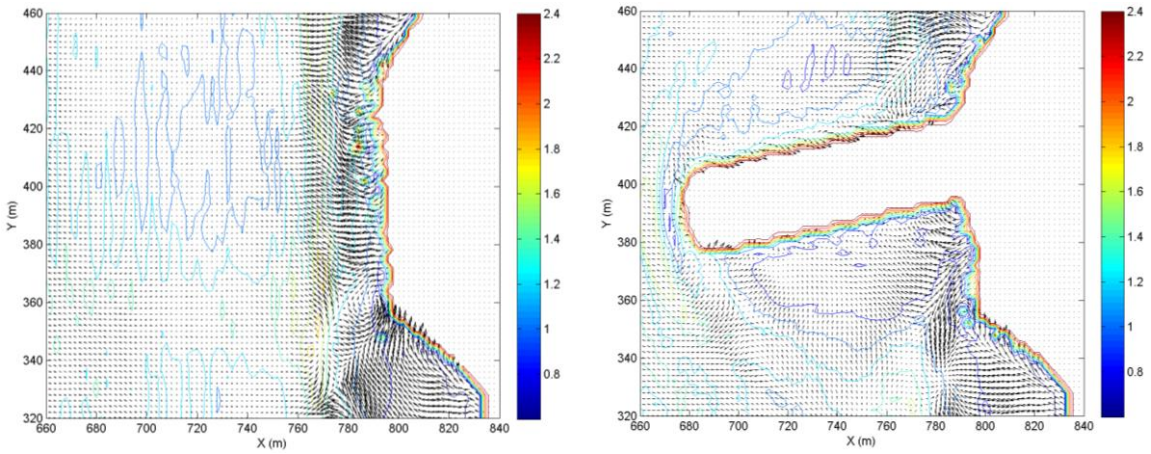

a) Horizontal velocity field: No groin run. b) Horizontal velocity field: Control groin run.

Fig. 16 – Mean horizontal velocity field in a small area (180x140 m^2) of the domain surrounding the groin: a) No-groin scenario and b) Control scenario. Quiver plots automatically stretch the velocity arrows to fit within the grid and thus only represent the direction of velocity vectors and their relative length. The arrows were augmented by a factor of 3 for better visualization. Colour contours represent Hs (m).

6.3. Other scenarios

After analysing the change of Hs and horizontal velocity imparted by a single 200 m-long groin, with a 10º orientation, considering an incident wave with 1.0 m, and a tide concomitant with a sea-surface level of 0.50 m, this study proceeds to the investigation of the different impacts that a groin would have, if its structural configuration was altered, or hydrodynamic conditions were different. All the new scenarios are compared to control-groin scenario, henceforward considered the control scenario.

6.3.1. Different groin length

To evaluate the impact of changing groin length, three new groin lengths of L=250 m, L=300 m and L=400 m were studied. Groin orientation, wave conditions and sea-surface level were considered the same as in the control run. The percentage relative Hs differences between each run and the control run were considered significant when greater than 7.5%, since no differences greater than 10% were observed.

From Fig. 17 it is evident that as the length of the groin increases, the impact on the significant wave height extends further in the domain, and reflection phenomena due to the reflective upper and lower boundaries of the domain appear to become more significant. Breaking events, in the control run mostly concentrated near the head of the groin, for longer groins, extend further to both sides of the head, and towards the shoreline in the lee-side of the groin. In the case of the 400 m-long groin, breaking events start closer to the shore than the groin tip. The shadow-zone on the lee-side also gets wider, with lower wave heights.

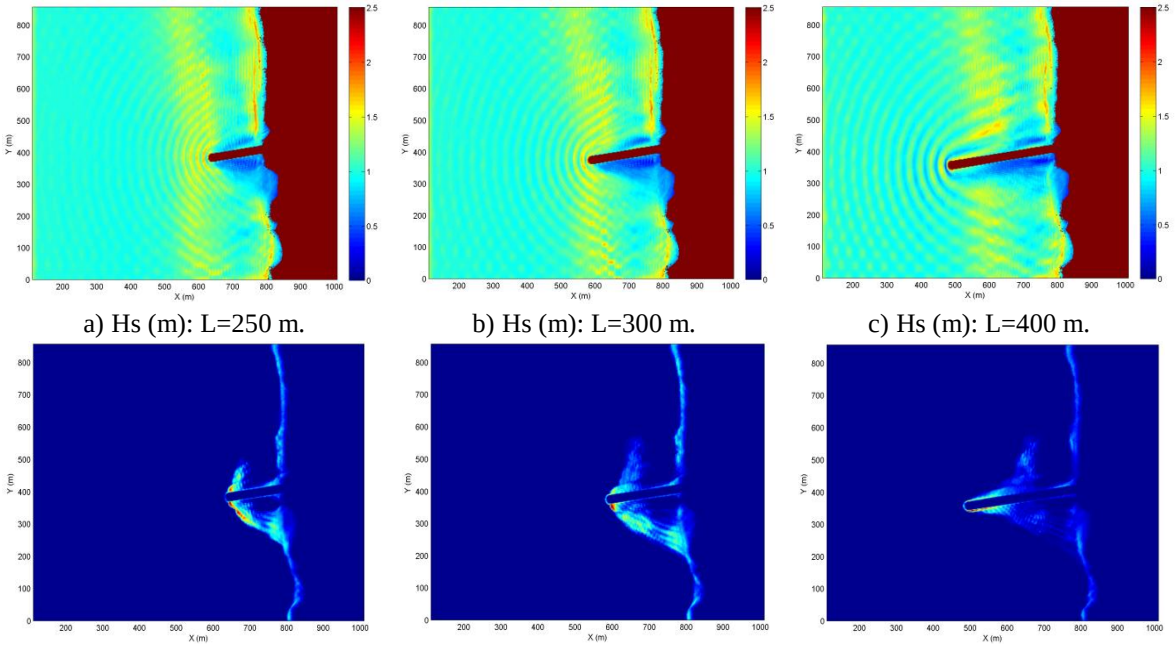

a) Hs (m): L=250 m. b) Hs (m): L=300 m. c) Hs (m): L=400 m.

d) Wave breaking: L=250 m. e) Wave breaking: L=300 m. f) Wave breaking: L=400 m.

Fig. 17 – Colour maps of Hs (top line) and wave breaking locations (bottom line) in the domain, for L=250 m, respectively a) and d), L=300 m, respectively b) and e) and L=400 m, respectively c) and f).

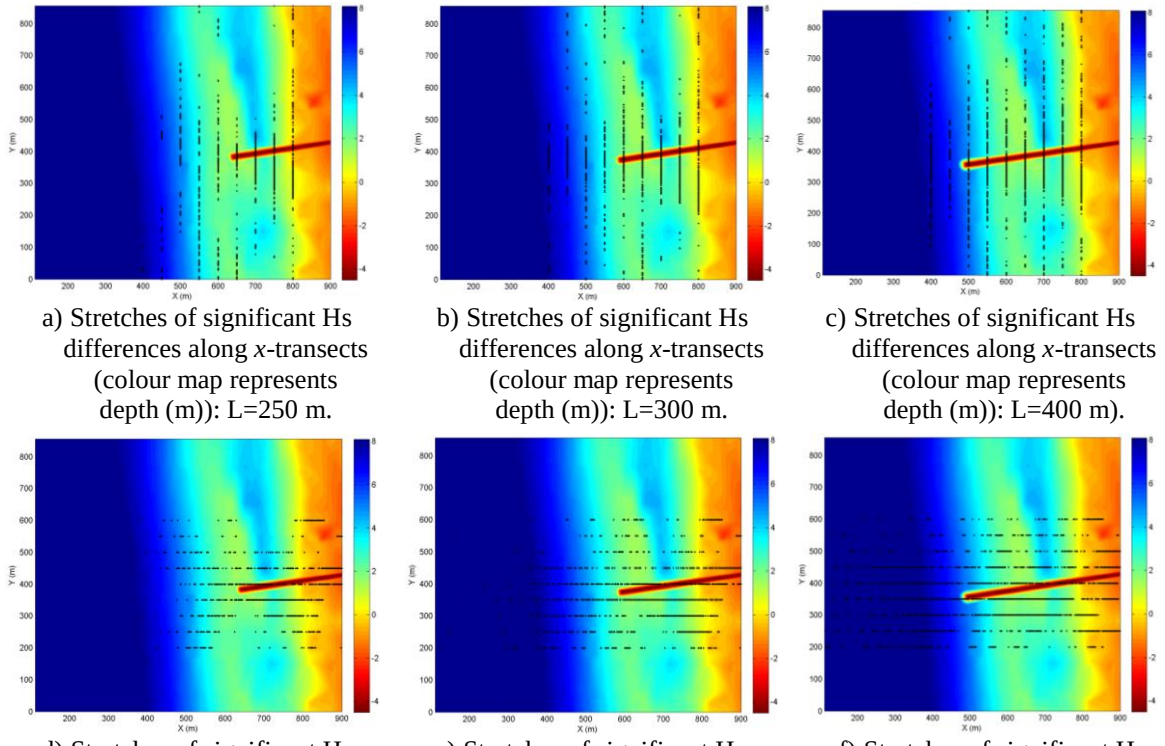

a) Stretches of significant Hs differences along *x*-transects (colour map represents depth (m)): L=250 m.

b) Stretches of significant Hs differences along *x*-transects (colour map represents depth (m)): L=300 m.

c) Stretches of significant Hs differences along *x*-transects (colour map represents depth (m)): L=400 m).

d) Stretches of significant Hs differences along *y*-transects (colour map represents depth (m)): L=250 m.

e) Stretches of significant Hs differences along *y*-transects (colour map represents depth (m)): L=300 m.

f) Stretches of significant Hs differences along *y*-transects (colour map represents depth (m)): L=400 m.

Fig. 18 – Stretches of the transects where the Hs differences between each run and the control run are greater than 7.5%, along x – a), b) and c) – and y – d), e) and f) - transects, for L=250 m (left column), L=300 m (central column) and L=400 m (right column).

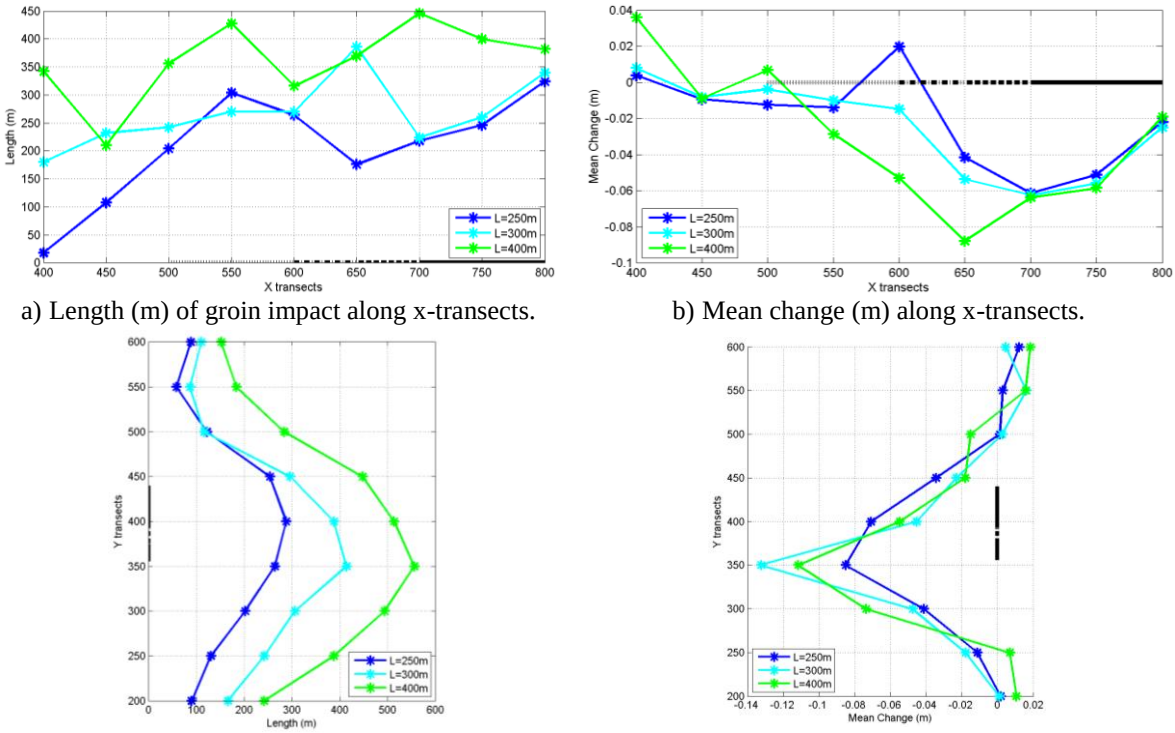

a) Length (m) of groin impact along x-transects.

b) Mean change (m) along x-transects.

c) Length (m) of groin impact along y-transects.

d) Mean change (m) along y-transects.

Fig. 19 – a) and c) Length of the stretches of the transects where the Hs differences between each run and the control run are greater than 7.5%, for each transect, respectively along *x* and *y*. b) and d) Mean change (m) (differences between each run and the control run), respectively along *x* and *y*.

Fig. 18 and Fig. 19 expose the impact of increasing groin length on Hs values. Significant differences between each scenario and the control scenario become more wide-spread over the domain, although the dominance of the influence in the closest vicinity of the groin remains. For the L=400 m groin, these differences extend as far as the left boundary of the domain. The length of the significant differences stretches generally decreases from the shoreward-end of each groin, towards its head. An increase of this length, evident for x=550 m, for both L=250 m and L=400 m groins and for x=650 m, for L=300 groin (in Fig. 19a), could be either related to the position of the submerged bar (located at about x=600m), where the first abrupt depth change occurs, hence justifying the greater impact of the groin, or to the position of the head of the groin. Along the y-transects, a more predictable behaviour is found, with the significant differences in Hs stretching longer in the transects closer to the groin, with a maximum in the transect that crosses the head. Mean change follows a similar tendency along y-transects, with Hs further decreasing as groin length increases. For depths shallower than the bathymetric trough, mean change increases, with Hs progressively diminishing, but thenceforth it generally decreases.

A general tendency of increasing impact lenght and mean change follows the increasing of groin length, as well as a slight shift of this impact further to the lee-side of the groin. Although no solid conclusions can be drawn on the importance of the bar and trough positions, results might point to the importance of these features on the impact different groins can have on Hs.

6.3.2. Different groin orientation

After analysing the impact of varying the length of the groin, the impact of changing groin orientation is explored. Hence, three groin orientations, ϕ=15º, ϕ=25º and ϕ=30º were chosen. Groin length, wave conditions and sea-surface level were considered the same as in the control run. The percentage relative Hs differences between each run and the control run were considered significant when greater than 5%, since no differences greater than 10% or 7.5% were observed.

Fig. 20 presents the effect of increasing the angle between the shoreline-perpendicular and the groin. It becomes evident that the greater the angle, the greater the shadow-zone in the lee-side of the groin. For ϕ =15º, breaking still occurs mostly around the head of the groin, as in the control run. However, when ϕ suffers a 10º increase, breaking starts taking place mostly against the updrift side-slope of the groin, which will tend to increase reflection of the incident waves, that arrive roughly perpendicularly to the shoreline.

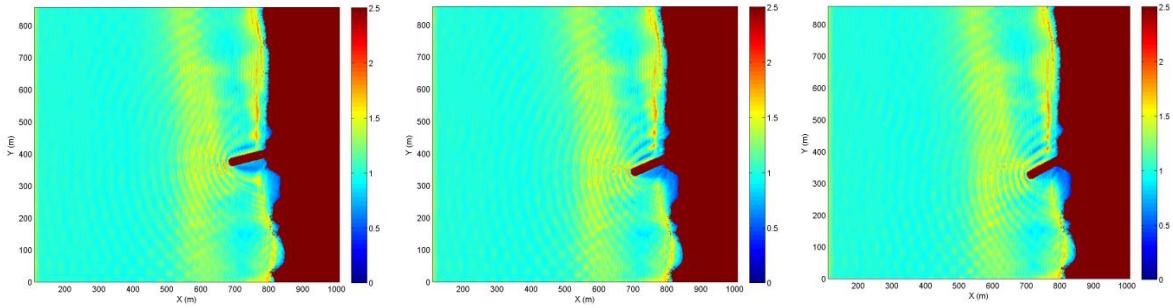

a) Hs (m): ϕ =15º. b) Hs (m): ϕ =25º. c) Hs (m): ϕ =30º.

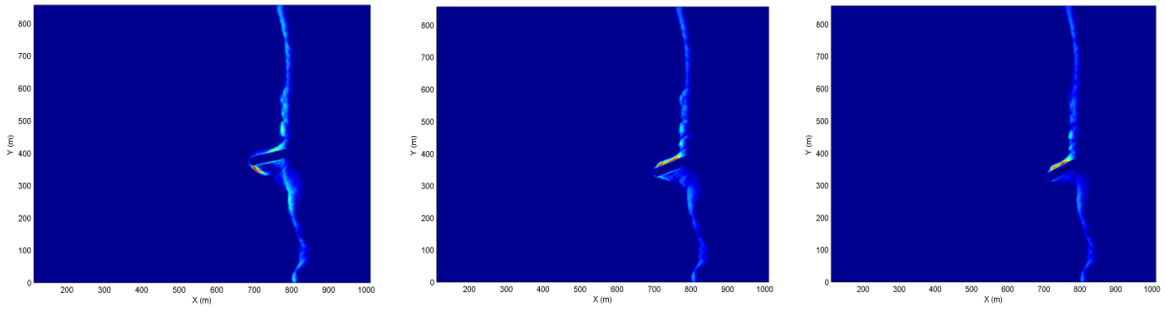

d) Wave breaking: ϕ =15º. e) Wave breaking: ϕ =25º. f) Wave breaking: ϕ =30º.

Fig. 20 – Colour maps of Hs (top line) and wave breaking locations (bottom line) in the domain, for ϕ=15º, respectively a) and d), ϕ=25º, respectively b) and e) and ϕ=30º, respectively c) and f).

Changing groin orientation implies changes in the extension (towards offshore) of the groin, the wave breaking locations and in phenomena such as diffraction and reflection. Hence, it becomes difficult to evaluate the specific impact of changing just the orientation (Fig. 21 and Fig. 22).

Generally, the length of the stretches in the transects where Hs differences greater than 5% happen, tends to be greater (in the *x*-direction), over the submerged bar, and near the groin, in its upper-side (in the *y*-direction). Hs mostly decreases, both along *x* and *y* directions, but increases along some transects, which is possibly related to the change in the wave breaking zones.

The relative difference between orientations is hard to interpret, since, and contrariwise to the changing of the other studied parameters, the differences between the control run and the three chosen scenarios do not seem to follow any specific and predictable pattern. Although for ϕ=15º

the length of groin impact along the transects is apparently longer than for greater values of ϕ (most likely because the groin extends further offshore in this case), the greatest values of mean change happen for ϕ=25º and ϕ=30º (possibly due to enhanced breaking or reflection and diffraction effects).

From the three scenarios chosen to evaluate the impact of groin orientation, the only conclusions that can be solidly drawn, is that the impact of changing groin orientation has a minor significance (no significant differences above 10% or 7.5% were observed) and that more scenarios would be necessary in order to better understand the effects of changing this specific parameter.

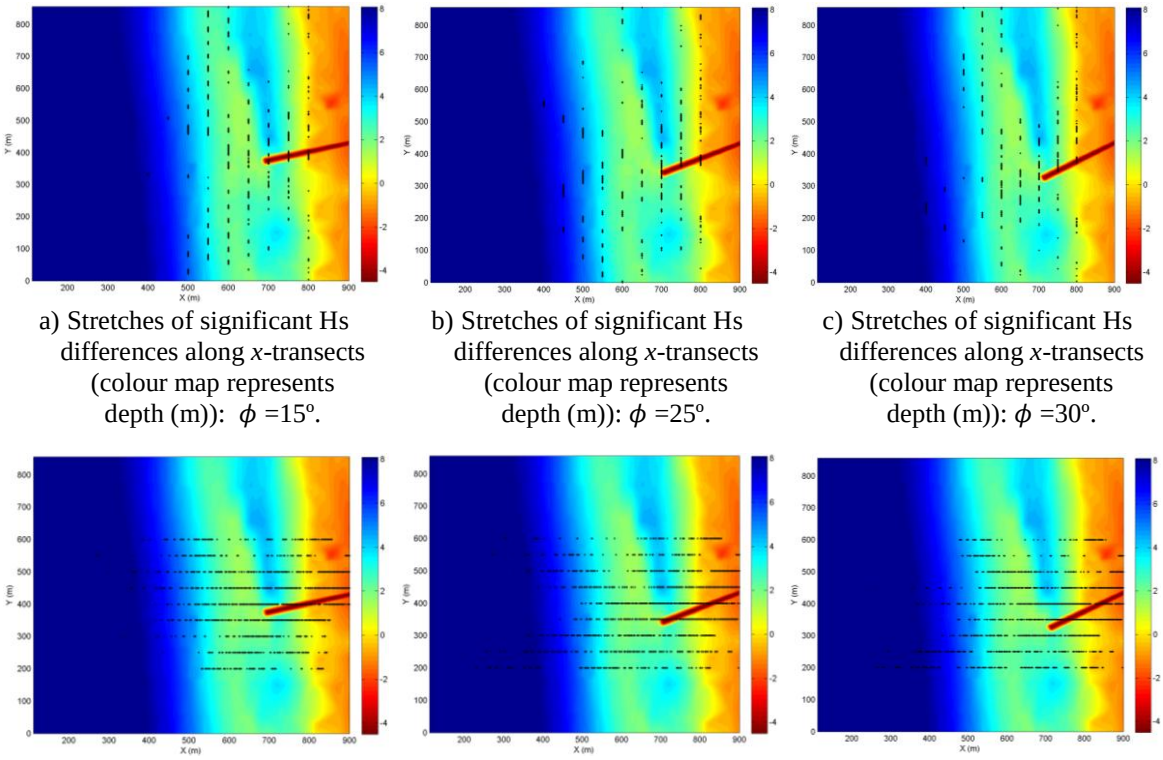

a) Stretches of significant Hs differences along *x*-transects (colour map represents depth (m)): ϕ =15º.

b) Stretches of significant Hs differences along *x*-transects (colour map represents depth (m)): ϕ =25º.

c) Stretches of significant Hs differences along *x*-transects (colour map represents depth (m)): ϕ =30º.

d) Stretches of significant Hs differences along *y*-transects (colour map represents depth (m)): ϕ =15º.

e) Stretches of significant Hs differences along *y*-transects (colour map represents depth (m)): ϕ =25º.

f) Stretches of significant Hs differences along *y*-transects (colour map represents depth (m)): ϕ =30º.

Fig. 21 – Stretches of the transects where the Hs differences between each run and the control run are greater than 5%, along *x* – a), b) and c) – and y – d), e) and f) – transects, for ϕ =15º (left column), ϕ =25º (central column) and ϕ =30º (right column).

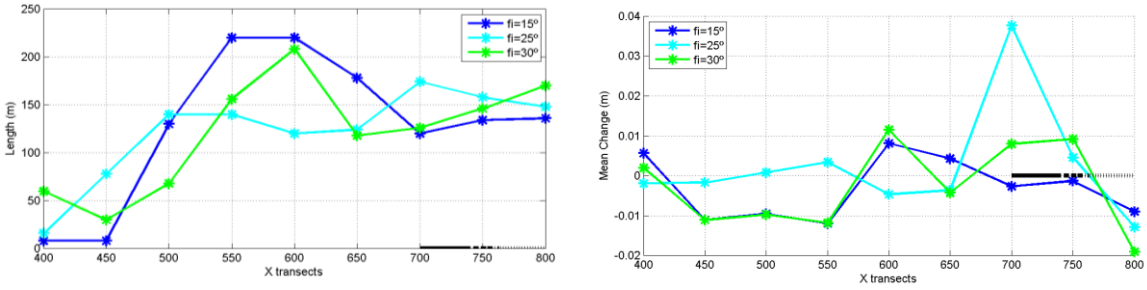

a) Length (m) of groin impact along x-transects.

b) Mean change (m) along x-transects.

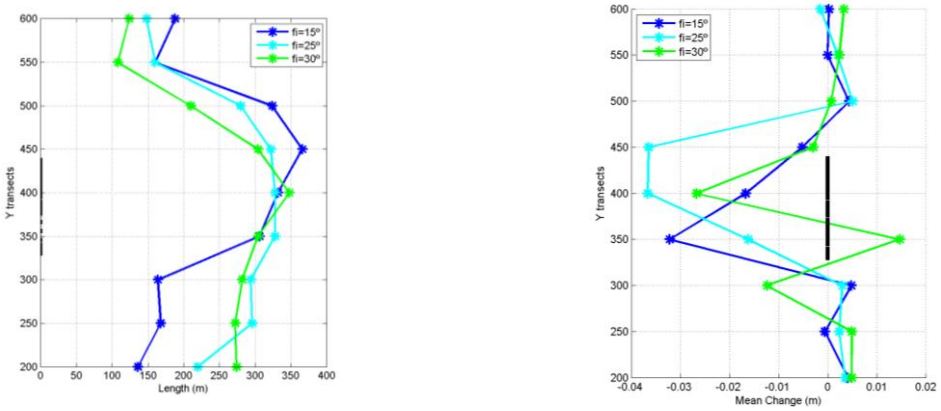

c) Length (m) of groin impact along y-transects. d) Mean change (m) along y-transects.

Fig. 22 – a) and c) Length of the stretches of the transects where the Hs differences between each run and the control run are greater than 5%, for each transect, respectively along *x* and *y*. b) and d) Mean change (m) (differences between each run and the control run), respectively along *x* and *y*.

6.3.3. Different significant incident-wave height

In addition to groin configuration, also the incident wave conditions are an important factor to account for when evaluating groin impact on significant wave height. Hence, to understand the influence of the significant height of the incident waves, three different incident significant wave heights were chosen: Hs=1.5 m, Hs=2.0 m and Hs=3.0 m. Groin length and orientation and sea-surface level were considered the same as in the control run. The relative Hs differences between each run and the control run were considered significant when greater than 10%.

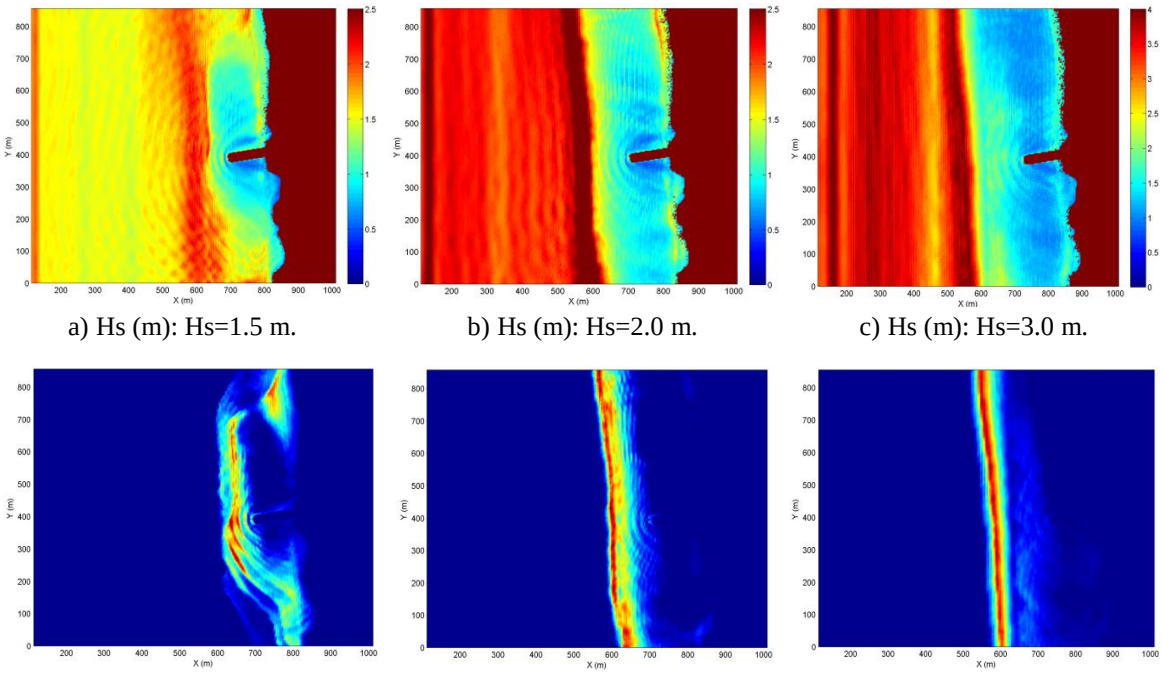

a) Hs (m): Hs=1.5 m. b) Hs (m): Hs=2.0 m. c) Hs (m): Hs=3.0 m.

d) Wave breaking: Hs=1.5 m. e) Wave breaking: Hs=2.0 m. f) Wave breaking: Hs=3.0 m.

Fig. 23 – Colour maps of Hs (top line) and wave breaking locations (bottom line) in the domain, for Hs=1.5 m, respectively a) and d), Hs=2.0 m, respectively b) and e) and Hs=3.0 m, respectively c) and f).

Fig. 23 evidences the impact of increasing the incident wave height on the significant wave height in the domain. As it would be expected, Hs increases in the whole domain (notice different colour scale of Fig. 23c), and breaking events occur further offshore. For incident waves with Hs=2 m and, particularly, Hs=3 m, wave breaking is no longer influenced by the groin, and diffraction and reflection phenomena induced by the groin become less relevant.

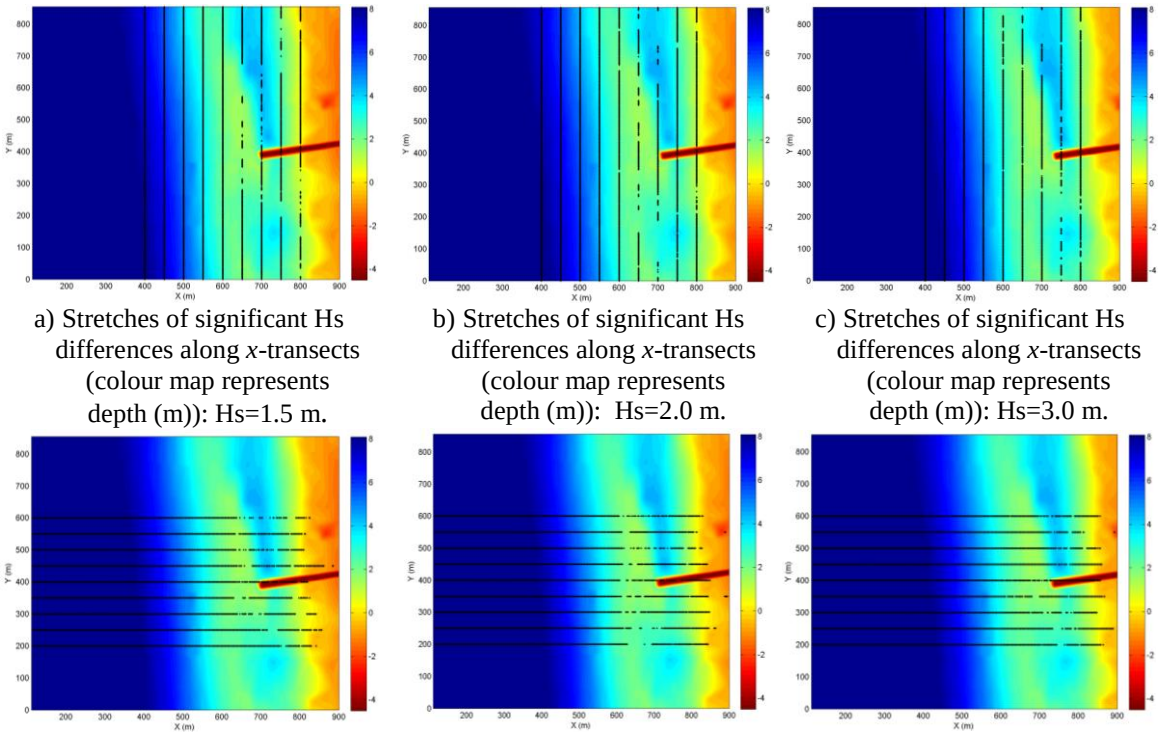

a) Stretches of significant Hs differences along *x*-transects (colour map represents depth (m)): Hs=1.5 m.

b) Stretches of significant Hs differences along *x*-transects (colour map represents depth (m)): Hs=2.0 m.

c) Stretches of significant Hs differences along *x*-transects (colour map represents depth (m)): Hs=3.0 m.

d) Stretches of significant Hs differences along *y*-transects (colour map represents depth (m)): Hs=1.5 m.

e) Stretches of significant Hs differences along *y*-transects (colour map represents depth (m)): Hs=2.0 m.

f) Stretches of significant Hs differences along *y*-transects (colour map represents depth (m)): Hs=3.0 m.

Fig. 24 – Stretches of the transects where the Hs differences between each run and the control run are greater than 10%, along *x* – a), b) and c) – and *y* – d), e) and f) – transects, for Hs=1.5 m (top line), Hs=2.0 m (central column) and Hs=3.0 m (bottom line).

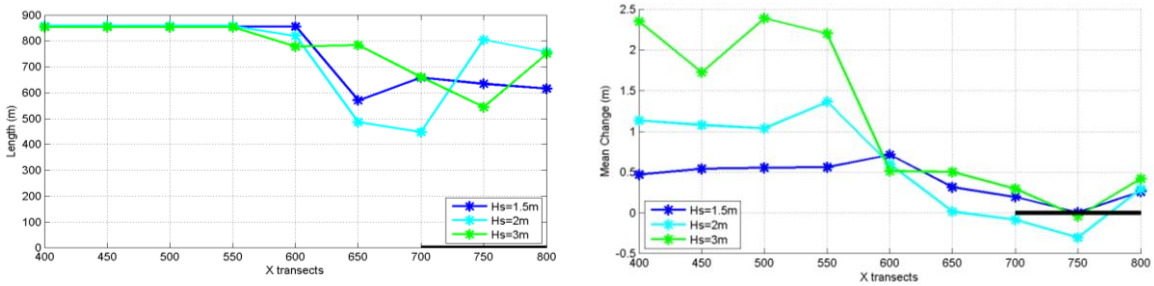

a) Length (m) of groin impact along x-transects.

b) Mean change (m) along x-transects.

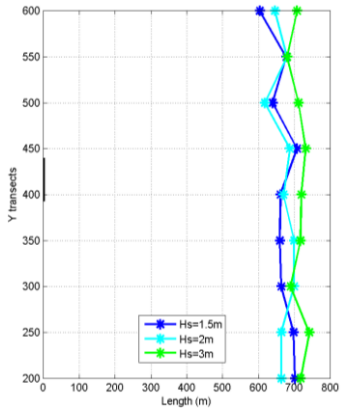

c) Length (m) of groin impact along y-transects.

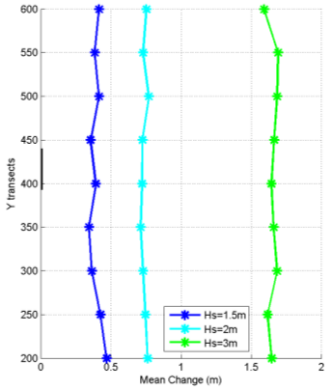

d) Mean change (m) along y-transects.

Fig. 25 – a) and c) Length of the stretches of the transects where the Hs differences between each run and the control run are greater than 10%, for each transect, respectively along *x* and *y*. b) and d) Mean change (m) (differences between each run and the control run), respectively along *x* and *y*.

Fig. 24 and Fig. 25 show that the impact of changing the incident significant wave height extends to almost the entire area of the domain covered by the transects. In the transects further offshore than the submerged bar, the percentage relative significant differences between each run and the control run are maximum for the three different-Hs scenarios. In the transects closer to shore, the length of significant differences along the transects is mostly greater for Hs=3 m, and for Hs=1.5 m and 2.0 m is quite similar. Mean change is straightforwardly greater as Hs increases, for *y*-transects and for the *x*-transects further offshore than the submerged bar, since these last are located at greater depths, where the process of shoaling is still starting, and hence the wave height input in the source is more relevant than for shallower locations, where the effects of shoaling already affect Hs. The *x*-transects located inshore the submerged bar exhibit a greater mean change for Hs=3 m, where the sheltering effect of the groin hardly affects Hs, which mostly increases compared to the control run. Nevertheless, the mean change significantly decreases in the transects near the groin for all the three scenarios and even presents negative values for Hs=2 m, due to the sheltering effect of the groin. For the y-transects, as mean change includes the change registered in the areas of the domain closer to the source, it shows a monotonic behaviour, increasing with increasing Hs, more markedly for Hs=3 m, since Hs=1.5 m and Hs=2 m scenarios have values of Hs input in the source closer to the control run.

Generally, the incident wave height has a quite significant impact on the Hs of the entire domain, which increases concomitantly with significant incident-wave height increase. In the transects closer to the shore, the Hs increase is attenuated by the groin.

6.3.4. Different sea-surface level

The last of the parameters to be considered is sea-surface level (which relates to tide level). Groin length and orientation and wave conditions were assumed the same as in the control run. The relative percentage Hs differences between each run and the control run were considered significant when greater than 10%.

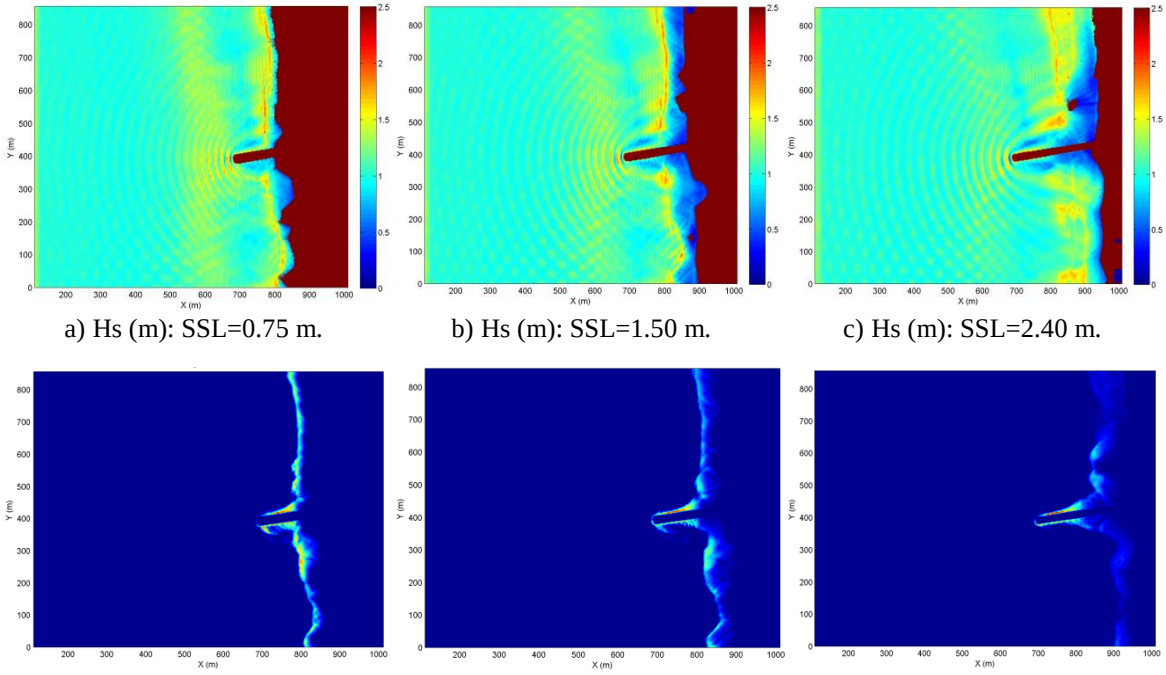

Fig. 26 – Colour maps of Hs (top line) and wave breaking locations (bottom line) in the domain, for SSL=0.75 m, respectively a) and d), SSL=1.50 m, respectively b) and e) and SSL=2.50 m, respectively c) and f).

The fact that the significant incident-wave height imposed in all three scenarios of Fig. 26 is 1.0 m, implies that breaking will always occur closer to shore than the head of the groin. However, it is still possible to observe that, for lower SSL, the breaking zone occurs closer to the head of the groin, and shifts towards closer to shore as SSL rises. When SSL is higher (1.50 and 2.40 m), the wave breaking line, also denounced by the greatest Hs region of the domain, is pushed further away from the shoreline (over 100 m, in some places) and extends wider in the cross-shore direction than when SSL is lower.

Furthermore, it is notorious that the Hs augment cause by the submerged bar (for, approximately, x=600 m) is attenuated as SSL rises.

Fig. 27 and Fig. 28 show the clear tendency for the length of the stretches where relative percentage differences greater than 10% occur to increase as SSL rises. It is also visible the influence of the submerged bar position in the length of the stretches: the greatest lengths, with an exception for the two transects closer to the shore, are calculated for the transects that follow the shallower depths of the submerged bar. The two exception transects are located very close to, and even over the shoreline, and hence SSL has a stronger immediate impact, since it conditions the position of the shoreline itself. The influence of the groin is also evident in its vicinity, particularly along y-transects, where significant differences cover greater stretches in the transects that cross the groin and are closer to it.

The mean change, for SSL=0.75 m, is very small, since in this scenario SSL only differs from the control run by 0.25 m. As this difference attains more negative values, for SSL=1.50 m and SSL=2.40 m scenarios, Hs decreases, mostly over the submerged bar, especially for the higher SSL. This change is again more relevant closer to the shoreline. The greater mean change, in the transect x=800 m, relates to the fact that for lower SSL this transect was mostly located inland and

as SSL rises, it becomes covered with water, which thus results in greater Hs. Along the *y*-direction, mean change is around one order of magnitude smaller and presents greater variations from transect to transect, particularly for the highest sea-surface level, although the general tendency for greater mean change when SSL is higher still remains. The mean change is related to the differences in every grid point of the transect between each SSL scenario and the control run, and so the presence of bathymetric features, such as the submerged bar and trough, affect each y-transect differently, which may justify the differences of mean change between consecutive transects. Also, along *y*-transects, mean change is predominantly positive, which indicates that, in average, Hs increases along the *y*-transects. Fig. 28 shows a wider breaking zone, where Hs is greater, for the scenarios with higher SSL, which might justify the mean Hs increase in these.

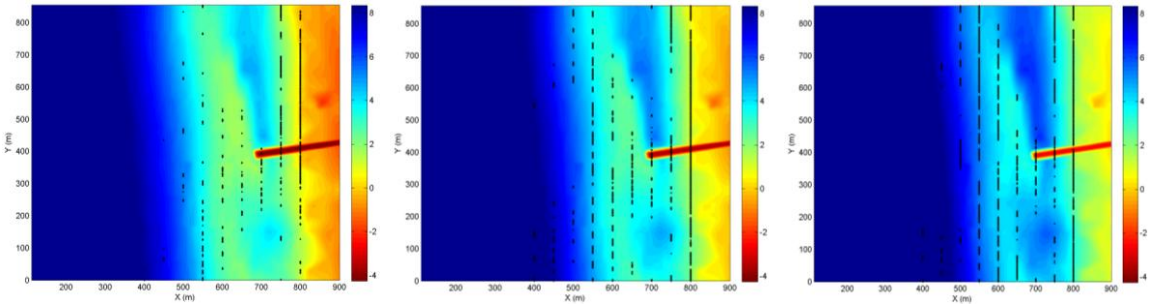

a) Stretches of significant Hs differences along *x*-transects (colour map represents depth (m)): SSL=0.75 m.

b) Stretches of significant Hs differences along *x*-transects (colour map represents depth (m)): SSL=1.50 m).

c) Stretches of significant Hs differences along *x*-transects (colour map represents depth) (m): SSL=2.40 m.

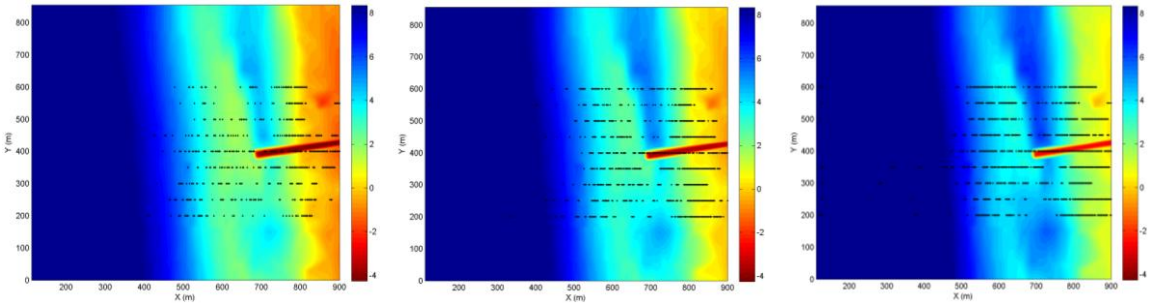

d) Stretches of significant Hs differences along *y*-transects (colour map represents depth (m)): SSL=0.75 m.

e) Stretches of significant Hs differences along *y*-transects (colour map represents depth (m)): SSL=1.50 m.

f) Stretches of significant Hs differences along *y*-transects (colour map represents depth (m)): SSL=2.40 m.

Fig. 27 – Stretches of the transects where the Hs differences between each run and the control run are greater than 10%, along *x* – a), b) and c) – and *y* – d), e) and f) – transects, for SSL=0.75 m (left column), SSL=1.50 m (central column) and SSL=2.40 m (right column).

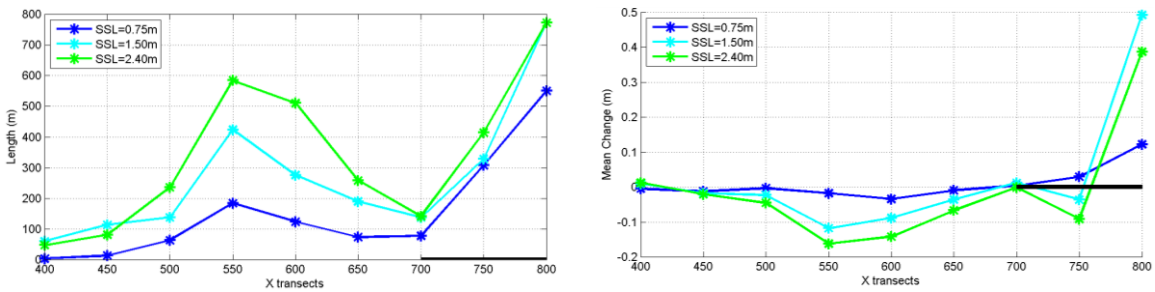

a) Length (m) of groin impact along *x*-transects.

b) Mean change (m) along *x*-transects.

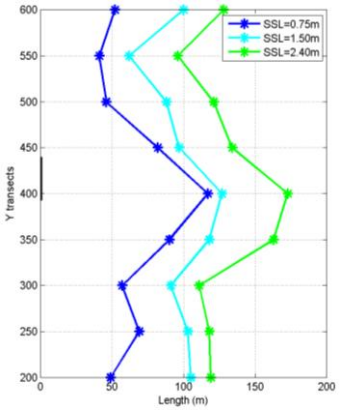

c) Length (m) of groin impact along *y*-transects.

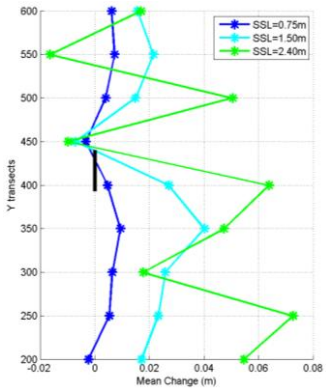

d) Mean change (m) along *y*-transects.

Fig. 28 – a) and c) Length of the stretches of the transects where the Hs difference between each run and the control run are greater than 10%, for each transect, respectively along *x* and *y*. b) and d) Mean change (m) (differences between each run and the control run), respectively along *x* and *y*.

6.3.5. Total impact of the four studied parameters

In order to better understand the relative impact of each of the four studied parameters, a comparative analysis is now presented. This impact is considered as the total length of every stretch of each transect, along *x*- and *y*-directions (respectively, Fig. 29a and Fig. 29b), where relative percentage differences of Hs between each scenario and the control run are greater than a threshold value, which varies accordingly to the parameter considered. The minimum-possible total length is zero for both *x*- and *y*-transects and the maximum-possible total length is 7722 m, for *x*-transects, and 8100 m for *y*-transects, both representing a sum of the length of all the nine transects in each direction, respectively.

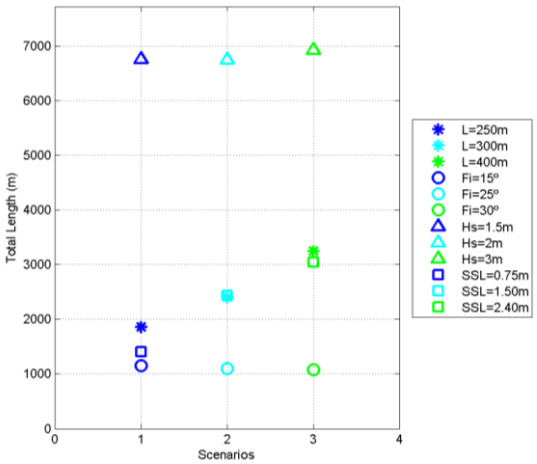

a) Total length of groin impact along *x*-transects, for each of the 3 scenarios considered for each parameter.

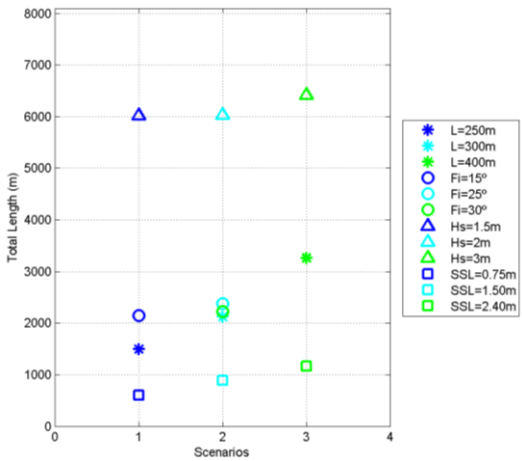

b) Total length of groin impact along *y*-transects, for each of the 3 scenarios considered for each parameter.

Fig. 29 – Total length of the stretches of the transects where the Hs differences between each run and the control run are greater than a threshold value (considered for each parameter) for each transect, respectively along *x* and *y* directions.

The purpose of Fig. 29 plots is to offer a qualitative comparative analysis of the impact of each parameter, than the actual absolute values of impact length. The numbers on the *x*-axis are merely indicative of the different scenarios.

Firstly, it should be remembered that both incident Hs and SSL impacts were calculated accounting for significant relative percentage differences of 10%, L impact was only relevant when differences were greater than 7.5% and ϕ determined the need of setting the lower limit of significant differences to 5%. Therefore, the environment factors, Hs and SSL, are significantly more important to correctly assess groin impact on the nearshore zone, followed by groin length and its orientation last.

The total length of the impact of changing the incident significant wave height is much greater than the impact of changing any of the other parameters and is more notorious along the x-transects (longshore direction) than along the y-transects (cross-shore direction).

The increase of wave height also results in an increase of the total length of the groin impact, more evident for the maximum Hs considered, of 3 m. From Fig. 29 it would appear that changing SSL results in a shorter length of groin impact than changing L or ϕ, but it is important to remember that the threshold for significant differences considered for SSL was greater than for those two parameters. Hence, SSL can be considered to have a significantly less important impact on significant wave height in the domain than the Hs parameter, but greater than L and ϕ. Furthermore, impact of changing sea-surface level is both globally and between scenarios greater in the longshore direction than its impact in the cross-shore direction. From one SSL scenario to the next, a linear increasing trend is found, as the SSL differs progressively more from the control-run SSL set as 0.50 m.

Although less important than environmental conditions, groin characteristics also have their share of impact on significant wave height in the domain. Firstly, and following a quite linear and similar trend in both *x*- and *y*-directions, the length of the groin has the greater impact, with differences becoming significant over the 7.5% threshold. The parameter that appears to have the smaller impact on significant wave height is the orientation of the groin. The response of Hs to the variation of ϕ is difficult to unravel, as it follows no apparent trend, and several factors that respond to changing orientation might be influencing that response. In the longshore direction, increasing ϕ seems to result in a lesser impact, whereas in the cross-shore direction an irregular trend is found between scenarios. More scenarios are due to be considered in order to better understand this particular impact.

7. CONCLUSIONS AND FUTURE IMPROVEMENTS

This thesis intended to bring further insight on groin impact on hydrodynamic conditions nearshore, by using a numerical wave propagation model COULWAVE. The model was applied to the field case of Cornélia beach, Costa da Caparica, to study wave propagation, shoaling, breaking and nonlinear effects associated. Afterwards, the impact on significant wave height and horizontal velocity in the domain of adding a groin to the original domain bathymetry was analysed, and several scenarios, with different groin lengths and orientations and different incident significant wave heights and sea-surface levels were explored. This work now draws to a close with some conclusions on COULWAVE ability to simulate wave propagation, shoaling and breaking and groin impact on significant wave height and, briefly, on horizontal velocity, in the study domain.

COULWAVE model seems to be fairly able of simulating well the field data, particularly the values of Hs. For Ts, differences between numerical and field data are greater. As it would be expected, for the instrument located on the wave-source position of the model, the model simulates almost exactly the input field data. As it gets closer to the shore and nonlinear phenomena become relevant, the results simulated by the model tend to diverge more from field data, especially for locations after wave breaking. On a spectral level, the model is capable of simulating the most energetic frequencies. Since the model was forced with monochromatic waves, it presents a greater difficulty in simulating energy dispersion to other frequencies, of lower or higher energy than the higher-energy ones. However, some dispersion is still simulated, as well as some energy bursts observed along the interval spectrally analysed.

For the horizontal velocity, the order of magnitude of instrumental data is well represented, but the model seems less able to describe the general trend, exhibiting numerical data a greater oscillation between consecutive 30-min intervals of maximum, minimum, mean and root-mean-square velocities (for both cross-shore and longshore components) than field data.

Furthermore, for Hs, Ts and horizontal velocities the model efficiently simulates the influence of the tidal cycle in the results, denouncing the approximately 12h intervals between high-tides, when the two instruments closer to the shore are submerged and are operational to measure Hs, Ts and velocities.

Building a groin in a beach is expected to lead to changes in wave conditions and the horizontal velocity field nearshore. Diffraction, refraction and reflection phenomena acquire a greater relevance in the domain and wave breaking locations tend to change. It should also be considered that the changes caused by the groin presence are specially felt on its lee-side and influence differently the nearshore region to each side of the groin.

The general tendency is of a significant wave height and velocity decrease in the longshore transects closer to shore than the head of the groin, particularly on its lee-side, where the shadow-zone has a sheltering effect on wave conditions. Contrariwise, in the closest vicinity of the groin tip, wave height tends to increase, together with velocity. The velocity tends to be directed towards the shore near breaking regions, and seawards away from these regions, since a weak undertow is the most relevant cross-shore velocity simulated by the model when no breaking is present.

The main conclusion of the present work is that the environmental factors, incident wave height, Hs, and sea-surface level, SSL, are significantly more important to correctly assess groin impact on nearshore hydrodynamics, followed by the structural factors, the length of the groin, L, and its orientation, ϕ, at last.

Hence, if a groin were to be built anywhere, firstly, the most common wave conditions should be considered, since the variation of significant incident-wave height imparts the greater changes in wave height nearshore, where the groin would be located. If the typical wave heights exceed a certain height, the groin effect might not be so important in wave breaking locations. Then, the typical tidal range should be evaluated, since a small 2 m change in sea-surface level can cause great depth changes over bathymetric features and thus influence wave propagation. Both these two environmental factors will have a severe influence on the wave breaking locations, which will then further condition wave height and horizontal velocities.

When the typical breaking locations for different wave conditions and tide levels are studied, it is important to define groin characteristics, in order to obtain the best results on shoreline protection. Different lengths are to be considered, seen that the greater the length, the greater the sheltering effect expected, and extending further to the lee-side of the groin. The impact will also reach a broader region of the domain. At last, with a smaller verified impact on wave conditions,

the best orientation of the groin is hard to unravel. Since it influences other factors, such as groin extension towards offshore, and reflection and diffraction phenomena, it becomes difficult to correctly assess the impacts of changing groin orientation, and results show an apparently almost-random behaviour. More groin orientations should be considered for a better understanding of the influence of this parameter.

Hereupon, future improvements could help overcoming some of the current limitations of this work.

Particularly, relatively to COULWAVE limitations, it is important to underline that the application of the model to bottom slopes of about 1/6 can be critical, since its fundamental equations are integrated assuming gently-sloping bottoms. This justifies the difficulty of the model to simulate all the initially chosen groin scenarios, which had to be progressively adapted until a convenient set of scenarios possible of being simulated by the model without "crashing" was defined. The excluded scenarios that "crashed" had the common aspect that breaking would occur too close to the front of the head of the groin, which can thus lead to the supposition that the problem was a consequence of the abrupt slopping of bathymetry caused by the extension of the groin to greater depths. A possible solution for this problem, so that simulating a wider range of scenarios would become viable, would be using a more recent version of the model, V. 2.0, which allows the use of a finite volume method for the derivatives, resulting in a more stable model that is then capable of dealing with greater bathymetric changes. This is, however, expected to significantly increase computational time cost.

Furthermore, phenomena such as wave breaking are included in the model through the addition, to the original equations, of a turbulent viscosity term, which depends on a set of parameters, related to the onset, duration and cessation of breaking events, that should be calibrated for each single case study and wave condition imposed, and were kept constant for all the simulated 30-min intervals used to compare the model results with field data. So a sensitivity study for each 30-min intervals on the wave breaking parameters should be considered.

Another great limitation of this work is the presupposition of incident wave direction exclusively perpendicular to the coast. The fact that the field instruments were not capable of measuring wave direction limited imposition of wave direction in the model and calibration of this parameter. Hence, exploring the influence of incident waves direction in wave propagation and breaking, and its relation with groin impact should bring further improvements to the study. It would also be interesting exploring the forcing of the model with irregular waves, in order to increase the proximity of the results to field data.

When the differences between each scenario and the control run where calculated, an absolute value was assumed, and thus the relation of those differences with increasing or decreasing Hs was not considered, and only the change of Hs was analyzed, without specifically being scrutinized if that change was either positive (Hs increase) or negative (Hs decrease). Carrying this analysis further could help understand the origin of such changes in each region of the domain.

Moreover, the study of groin impact for different scenarios was only done for Hs, and the investigation of groin impact in the horizontal velocity field in each scenario would also be an important improvement to this work.

Finally, the greatest further improvement for this thesis would be carrying through the analysis of the changes of Hs and horizontal velocities under different scenarios, to evaluate alterations in the sediment transport nearshore, and then model shoreline change in different situations.

Nevertheless, from a general perspective, the proposed aims were attained, and COULWAVE wave propagation, shoaling and breaking results were obtained for Cornélia beach, in Costa da Caparica site and this model was further applied to the study of groin impact on significant wave height and, briefly, on horizontal velocity, in the domain.

REFERENCES

Basco, D. R. (2006). Shore Protection Projects. *Coastal Engineering Manual*, U.S. Army Corps of Engineers. Washington, DC. 59-76.

Bezerra, M. and Ferreira, O. (2010). Relatório de campo – Universidade do Algarve. Projecto BRISA - Campanha da Costa da Caparica (Praia da Saúde) (11 a 15 de Maio de 2010).

Boussinesq, J. (1872). Théorie des ondes et des remous qui se propagent le long d'un canal rectangulaire horizontal, en communiquant au liquide contenu dans ce canal des vitesses sensiblement pareilles de la surface au fond. *Journal de Mathématiques Pures et Appliquées*, **17** (2): 55-108.

Bowen, A. J. and Inman, D. L. (1969). Rip currents 2. Laboratory and field observations. *Journal of Geophysical Research - Oceans*, **74** (23): 5479–5490.

Cavaleri, L., Alves, J.-H., Ardhuin, F., Babanin, A., Banner, M., Belibassakis, K., Benoit, M., Donelan, M., Groeneweg, J., Herbers, T. H. C., Hwang, P., Janssen, P., Janssen, T., Lavrenov, I., Magne, R., Monbaliu, J., Onorato, M., Polnikov, V., Resio, D., Rogers, W., Sheremet, A., McKee Smith, J., Tolman, H. L., van Vledder, G., Wolf, J. and Young, I. (2007). Wave modelling - The state of the art. *Progress in Oceanography*, **75**: 603-674.

Chen, Q., Kirby, J. T., Dalrymple, R. A., Kennedy, A. B. and Chawla, A. (2000). Boussinesq modeling of wave transformation, breaking, and runup. II: 2D. *Journal of Waterway, Port, Coastal and Ocean Engineering*, **126**: 48-56.

Chen, Q., Kirby, J. T., Dalrymple, R. A., Shi, F. and Thornton, E. B. (2003). Boussinesq modeling of longshore currents. *Journal Geophysical Research*, **108** (C11): 3362.

Costa, M., Silva, R., Vitorino, J. (2001). Contribuição para o estudo do clima de agitação marítima na costa portuguesa. Instituto Hidrográfico.

Dean, R. G. (1978). Coastal structures and their interaction with the shoreline. *Application of Stochastic Processes in Sediment Transport*. Kikkaua, H. W. S. a. H., Water Resources Publications. Littleton, CO.

Dong, Z. and Zhan, J.-m. (2009). Numerical modeling of wave evolution and runup in shallow water. *Journal of Hydrodynamics, Ser. B*, **21** (6): 731-738.

Gourlay, M. R. (1974). Wave set-up and wave generated currents in the lee of a breakwater or headland. *Coastal Engineering 1974: Proceedings of the Fourteenth International Conference*, American Society of Civil Engineers, New York: 1976–1995.

Hansen, J. and Svendsen, I. (1979). Regular waves in shoaling water: experimental data. Technical report. ISVA Series, Paper 21.

Kennedy, A., Chen, Q., Kirby, J. and Dalrymple, R. (2000). Boussinesq modeling of wave transformation, breaking, and runup. Part I: 1D. *Journal of Waterway, Port, Coastal and Ocean Engineering*, **126** (1): 39-47.

Kirby, J., Wei, G., Chen, Q., Kennedy, A. and Dalrymple, R. (1998). FUNWAVE 1.0: Fully Nonlinear Boussinesq Wave Model Documentation and User's Manual. Center for Applied EngiCoastal Research, University of Delaware. 80 pp.

Korteweg, D. J. and deVries, G. (1895). On the change of form of long waves advancing in a rectangular channel, and on a new type of long stationary waves. *Philosophical Magazine*, **39** (5): 422-443.

Lynett, P. J., Wu, T.-R. and Liu, P. (2002). Modeling wave runup with depth-integrated equations. *Coastal Engineering*, **46**: 89-107.

Lynnet, P. and Liu, P. (2002). Modelling wave generation, evolution and interaction with depth-integrated, dispersive wave equations, *COULWAVE Code Manual*. Cornell University Long and Intermediate Wave Modelling Package.

Lynnet, P. and Liu, P. (2004). Modelling wave generation, evolution and interaction with depth-integrated dispersive wave equations, *COULWAVE Code Manual*. Cornell University Long and Intermediate Wave Modelling Package.

Madsen, P. A., Bingham, H. B. and Schaffer, H. A. (2003). Boussinesq-type formulations for fully nonlinear and extremely dispersive water waves: derivation and analysis. *Proceedings of the Royal Society of London*. **A 459**: 1075-1104.

Moura, T. (2010). Aplicação da transformada de Hilbert-Huang para o estudo de ondas medidas por PUV. MSc Thesis, Civil Engineering Department, UFRJ/COPPE. 118 pp.

Nwogu, O. (1993). Alternative form of Boussinesq equations for nearshore wave propagation. *Journal of Waterway, Port, Coastal and Ocean Engineering*, **119** (6): 618-638.

Pattiaratchi, C., Olsson, D., Hetzel, Y. and Lowe, R. (2009). Wave-driven circulation patterns in the lee of groynes. *Continental Shelf Research*, **29**: 1961-1974.

Peregrine, D. H. (1967). Long waves on a beach. *Journal of Fluid Mechanics*, **27**: 815-827.

Press, W., Flannery, B. and Teukolsky, S. (1989). Numerical Recipes. Cambridge University Press.569-572.

Shi, F. and Kirby, J. T. (2005). Curvilinear parabolic approximation for surface wave transformation with wave–current interaction. *Journal of Computational Physics*, **204**: 562–586.

Taveira, D. (2010). Características da ondulação na praia de Faro. BSc Thesis, Physics Department, University of Aveiro. 48 pp.

U. S. Army Corps of Engineers (1992). Coastal groins and nearshore breakwaters, *Engineering and Design*. Department of the Army, U.S. Army Corps of Engineers, Washington, D.C. 91 pp.

Watts, P., Grilli, S. T., Kirby, J. T., Fryer, G. J. and Tappin, D. R. (2003). Landslide tsunami case studies using a Boussinesq model and a fully nonlinear tsunami generation model. *Natural Hazards and Earth System Sciences*, **3**: 391–402.

Wei, G. and Kirby, J. (1995). A time-dependent numerical code for extended Boussinesq equations. *Journal of Waterway, Port, Coastal and Ocean Engineering*, **120**: 251-261.

Wei, G., Kirby, J. T., Grilli, S. T. and Subramanya, R. (1995). A fully nonlinear Boussinesq model for surface waves. Part 1. Highly nonlinear unsteady waves. *Journal of Fluid Mechanics*, **294**: 71-92.

Willmott, C., Ackleson, S., Davis, R., Feddema, J., Klink, K., Legates, D., O'Donnell, J. and Rowe, C. (1985). Statistics for the evaluation and comparison of models. *Journal of Geophysical Research*, **90** (C5): 8995-9005.